

RXJ0848.6+4453: THE EVOLUTION OF GALAXY SIZES AND STELLAR POPULATIONS IN A $Z = 1.27$ CLUSTER

INGER JØRGENSEN¹, KRISTIN CHIBOUCAS¹, SUNE TOFT², MARCEL BERGMANN³, ANDREW ZIRM², RICARDO P. SCHIAVON^{1,4}, RUTH GRÜTZBAUCH⁵

¹Gemini Observatory, 670 N. A'ohoku Pl., Hilo, HI 96720, USA; ²Dark Cosmology Centre, Niels Bohr Institute, University of Copenhagen, Juliane Mariesvej 30, DK-2100 Copenhagen, Denmark; ³National Optical Astronomy Observatory, Tucson, AZ 85719, USA; ⁴Liverpool John Moores University, UK; ⁵Center for Astronomy and Astrophysics, University of Lisbon, Portugal

Submitted April 23, 2014. Accepted for publication in *Astronomical Journal*, August 2, 2014

ABSTRACT

RXJ0848.6+4453 (Lynx W) at redshift 1.27 is part of the Lynx Supercluster of galaxies. We present an analysis of the stellar populations and star formation history for a sample of 24 members of the cluster. Our study is based on deep optical spectroscopy obtained with Gemini North combined with imaging data from *Hubble Space Telescope*. Focusing on the 13 bulge-dominated galaxies for which we can determine central velocity dispersions, we find that these show a smaller evolution with redshift of sizes and velocity dispersions than reported for field galaxies and galaxies in poorer clusters. Our data show that the galaxies in RXJ0848.6+4453 populate the Fundamental Plane (FP) similar to that found for lower redshift clusters. The zero point offset for the FP is smaller than expected if the cluster's galaxies are to evolve passively through the location of the FP we in our previous work established for $z = 0.8 - 0.9$ cluster galaxies and then to the present day FP. The FP zero point for RXJ0848.6+4453 corresponds to an epoch of last star formation at $z_{\text{form}} = 1.95^{+0.22}_{-0.15}$. Further, we find that the spectra of the galaxies in RXJ0848.6+4453 are dominated by young stellar populations at all galaxy masses and in many cases show emission indicating low level on-going star formation. The average age of the young stellar populations as estimated from the strength of the high order Balmer line $H\zeta$ is consistent with a major star formation episode 1-2 Gyr prior, which in turn agrees with $z_{\text{form}} = 1.95$. These galaxies dominated by young stellar populations are distributed throughout the cluster. We speculate that low level star formation has not yet been fully quenched in the center of this cluster maybe because the cluster is significantly poorer than other clusters previously studied at similar redshifts, which appear to have very little on-going star formation in their centers. The mixture in RXJ0848.6+4453 of passive galaxies with young stellar populations and massive galaxies still experiencing some star formation appears similar to the galaxy populations recently identified in two $z \approx 2$ clusters.

Subject headings: galaxies: clusters: individual: RXJ0848.6+4453 – galaxies: evolution – galaxies: stellar content.

1. INTRODUCTION

Recent results regarding stellar populations and sizes of galaxies at redshifts above one indicate that the redshift interval $z = 1 - 2$ spans the epoch during which major changes of galaxy properties took place. Some time during this epoch, the galaxy sizes change by a factor 3-5 (e.g., Toft et al. 2009, 2012; Newman et al. 2012; Cassata et al. 2013; van der Wel et al. 2014), major and minor merging takes place, triggering starbursts that then get quenched through processes as strangulation and ram-pressure stripping as the galaxies enter the dense environments of the cluster cores (Grützbauch et al. 2011; Quadri et al. 2012; Koyama et al. 2013). This results in the massive ($\text{Mass} > 10^{11} M_{\odot}$) passively evolving galaxies being in place by $z \approx 1$, while the lower mass galaxies continue to be added to the passive population as late as $z = 0.5$ (e.g., Sánchez-Blázquez et al. 2009). Massive clusters of galaxies have recently been found to redshift $z \approx 2$ (e.g., Stanford et al. 2012; Gobat et al. 2013). The current studies of these clusters are based primarily on photometry and limited redshift information, as very little high signal-to-noise spectroscopy exists of clusters galaxies with $z = 1 - 2$. However, the results have raised a number of questions fundamental to our understanding of galaxy evolution as it takes place in dense

environments:

1. At which epoch does the main size and structure evolution of cluster galaxies take place, and how is it linked to cluster properties (density, mass, virialization) and galaxy mass? Results at $z = 0.9$ (Jørgensen & Chiboucas 2013) and for $z = 1.6 - 2.1$ protoclusters (Zirm et al. 2012; Papovich et al. 2012; Strazzullo et al. 2013) suggest that the size evolution may be accelerated in dense cluster environments. However, Newman et al. (2014) in a study of a cluster at $z = 1.8$ find no difference between cluster and field galaxy sizes at this redshift.
2. When do the first low mass ($\text{Mass} < 10^{11} M_{\odot}$) galaxies populate the Fundamental Plane (FP) of passive galaxies (Djorgovski & Davis 1987; Jørgensen et al. 1996) as we observe it at $z < 1$? The prediction from our results for $z < 1$ clusters is that the low mass end of the FP is being populated at $z \approx 1 - 1.5$, while ages from the Balmer lines indicate a much earlier epoch for this process (Jørgensen et al. 2006, 2007; Jørgensen & Chiboucas 2013). Studies of stellar populations in cluster galaxies at $z > 1$ are needed to resolve this issue.
3. At which epoch and cluster density are the starbursts quenched leading to a large fraction of post-starburst galaxies, and subsequently to passive galaxies? Results for protoclusters at $z \approx 2$ show that the main transfor-

ijorgensen@gemini.edu, kchiboucas@gemini.edu
sune@dark-cosmology.dk, marcelbergmann@gmail.com
andrewzirm@gmail.com, R.P.Schiavon@ljmu.ac.uk
ruthregenborgen@gmail.com

mation must happen at $z = 1 - 2$ and depends on galaxy mass (Quadri et al. 2012; Koyama et al. 2013) and possibly also on the cluster environment (Tanaka et al. 2013).

Imaging data and deep spectroscopic data of cluster galaxies at $z \approx 1 - 2$ make it possible to address these questions in detail. With the installation of the red sensitive E2V Deep Depletion Charge-Coupled-Devices (E2V DD CCDs) in the Gemini Multi-Object Spectrograph on Gemini North (GMOS-N) it is now possible to obtain such spectra in the rest-frame blue and visible of galaxies up to $z \approx 1.3$. See Hook et al. (2004) for a detailed description of GMOS-N. For galaxies at higher redshift, such observations are becoming feasible with near-infrared multi-object spectrographs, e.g., the K-band Multi-Object-Spectrograph (KMOS) on the Very Large Telescope.

We have undertaken a project to obtain such deep spectroscopic observations of rich galaxy clusters at $z = 1 - 2$. In this paper we present the results from our first observations, addressing the outlined questions using new high signal-to-noise (S/N) spectra in the rest frame 3500-4400 Ångstrom for individual galaxies in the cluster RXJ0848.6+4453 (Lynx W) at $z = 1.27$. We analyze the spectroscopic data together with available *Hubble Space Telescope* (*HST*) imaging of the cluster obtained with the Advanced Camera for Surveys (ACS) in the filters F775W and F850LP.

The observational data are described in Section 2 and in the Appendix. In Section 3 we establish the cluster redshift and velocity dispersion as well as cluster membership for the observed galaxies. We also discuss mass of the cluster compared with masses of the other clusters included in the analysis. Section 4 gives an overview over the methods and models used in the analysis and defines the sub-samples of galaxies, which we refer to throughout the presentation of the results and the discussion. Our main results regarding evolution of size and velocity dispersions as well as stellar populations are described in Section 5. In Section 6 we discuss these results in the context of other recent results for galaxies at $z > 1$ as well as simple models for the evolution with redshift. The conclusions are summarized in Section 7.

Throughout this paper we adopt a Λ CDM cosmology with $H_0 = 70 \text{ km s}^{-1} \text{ Mpc}^{-1}$, $\Omega_M = 0.3$, and $\Omega_\Lambda = 0.7$.

2. OBSERVATIONAL DATA

2.1. Imaging of RXJ0848.6+4453

Ground-based imaging of RXJ0848.6+4453 was obtained primarily to show the performance gain provided by the replacing the original E2V CCDs in GMOS-N with E2V DD CCDs. This replacement was done in October 2011. Imaging of RXJ0848.6+4453 was obtained with the original E2V CCDs in October 2011 and repeated with the E2V DD CCDs in November 2011 (Table 1). For the results presented in this paper we made use of the imaging for the mask designs for the spectroscopy and to illustrate the spectroscopic sample (Figure 1). The imaging was done in the z' filter. For the observations with the original E2V CCDs the total exposure time was 60 min (obtained as twelve 5 min exposures) and the co-added image had an image quality of FWHM=0.52 arcsec measured from point sources in the field. For the E2V DD CCDs a total exposure time of 55 min obtained and the resulting image quality was FWHM=0.51 arcsec. As *HST/ACS* imaging in two filters is available of all galaxies in the spectroscopic sample, no other use is made of the ground-based

imaging.

Table 2 summarizes the *HST/ACS* data for the two fields used in this paper. Data are also available for a third field, covering Lynx E. However, as none of our spectroscopic sample galaxies are within that field these data are not used in the present paper. We also do not use the shallower imaging obtained for *HST* program ID 10496.

The *HST/ACS* data were processed as described in Chiboucas et al. (2009), using the drizzle technique (Fruchter & Hook 2002). The images were then processed with SExtractor (Bertin & Arnouts 1996). Total magnitudes $z_{\text{tot},850}$ were derived from the F850LP imaging. Aperture colors ($i_{775} - z_{850}$) were derived within an aperture with diameter of 0.5 arcsec. We used GALFIT (Peng et al. 2002) to fit $r^{1/4}$ profiles and Sérsic (1968) profiles to the galaxies in the spectroscopic sample and derive effective radii, magnitudes and surface brightnesses. This processing was done for the observations in F850LP only. The effective radii in Table 10 are derived from the semi-major and -minor axes as $r_e = (a_e b_e)^{1/2}$. The difference between the effective radii derived from the fits with the $r^{1/4}$ profiles and Sérsic profiles as expected correlates with the Sérsic index, see details in the Appendix. The median uncertainty on the Sérsic index is 0.1, with a few values up to 0.7 for galaxies with best fit indices larger than 4. As the Sérsic fits and indices in this paper are used primarily for selection of the bulge-dominated galaxies, these uncertainties do not affect our results significantly.

The photometry is calibrated to the AB system using the synthetic zero points for the filters, 25.654 for F775W, 24.862 for F850LP (Sirianni et al. 2005). Galactic reddening in the direction of the cluster is $E(B-V)=0.024$ (Schlafly et al. 2011), which gives, $A_{i_{775}} = 0.046$ and $A_{z_{850}} = 0.034$. The photometric parameters derived using SExtractor and GALFIT are listed in the Appendix, Table 10.

The photometry was calibrated to rest frame B-band. The calibration was established using stellar population models from Bruzual & Charlot (2003) as described in Jørgensen et al. (2005). The calibration is given in the Appendix.

2.2. Spectroscopy of RXJ0848.6+4453

The spectroscopic observations were obtained in multi-object spectroscopic (MOS) mode with GMOS-N, see Table 1 for the dates of the observations. The sample selection is based on the photometry from the *HST/ACS* imaging. Figure 2 shows the color-magnitude (CM) relation for the field. Galaxies were selected to maximize the coverage along the red sequence from the brightest cluster galaxy (BCG) to $z_{\text{tot},850} \approx 24.5$ mag. The triple merger (red star on Fig. 1), which is considered the BCG, was not included in the observations. This decision was made in part because it would eliminate another known bright cluster member from the mask and in part because the angular separation of the components is only ≈ 0.5 arcsec making it very difficult to separate them in ground-based spectroscopy obtained in natural seeing. Priority was given to galaxies within 0.1 mag of the CM relation in ($i_{775} - z_{850}$) versus $z_{\text{tot},850}$. Additional space in the mask was filled with galaxies with ($i_{775} - z_{850}$) > 0.5 and $z_{\text{tot},850}$ in the interval from 21 mag to 25 mag. Some of these turned out to be blue cluster members. The spectroscopic sample is marked on Figures 1 and 2. Two blue stars were included in the mask in order to obtain a good correction for the telluric absorption lines. The blue stars are also marked on Figure 1.

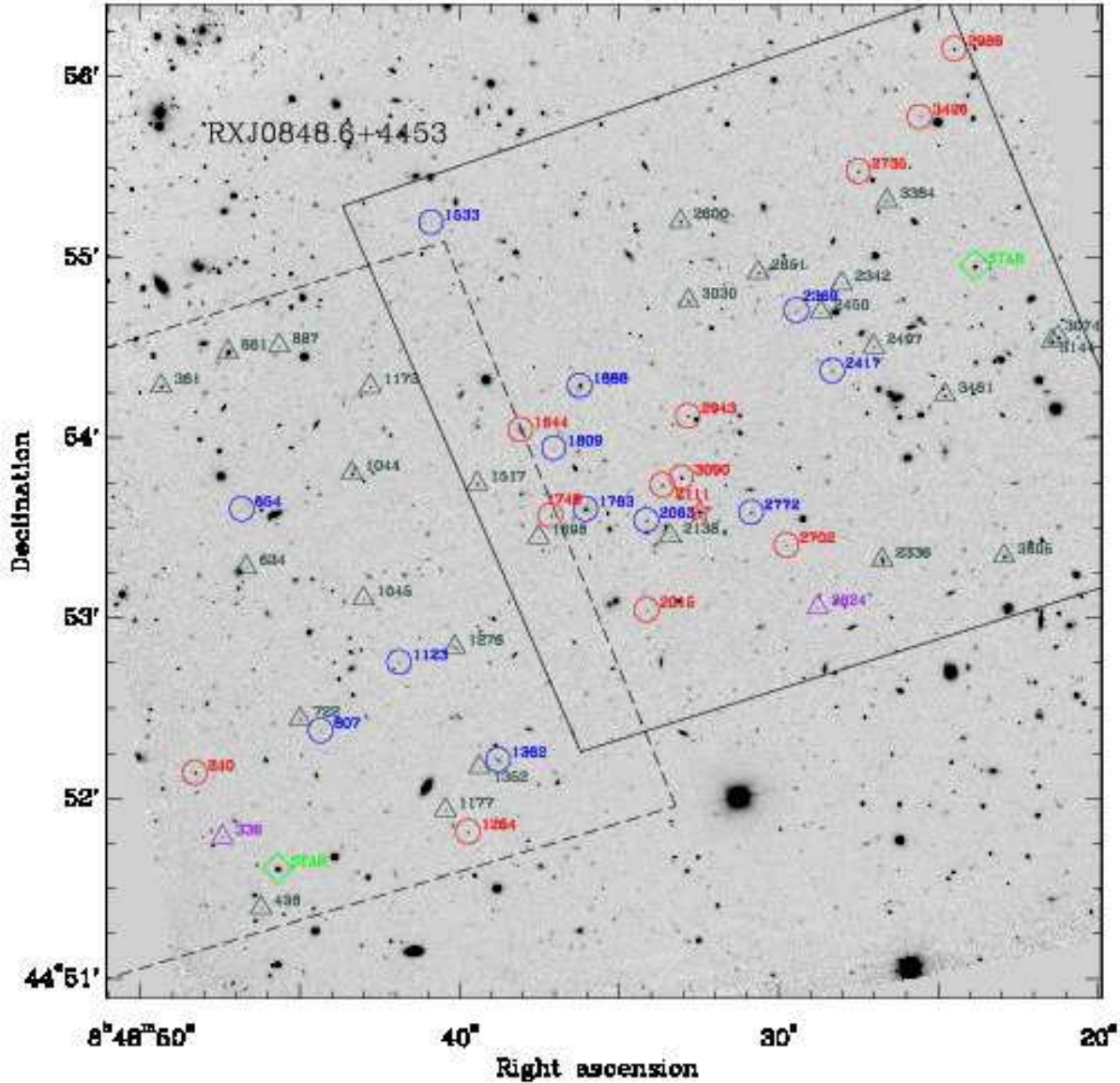


Figure 1. GMOS-N z' -band image of RXJ0848.6+4453 with our spectroscopic sample marked. Red circles – confirmed members with $EW[O II] \leq 5 \text{ \AA}$. Blue circles – confirmed members with $EW[O II] > 5 \text{ \AA}$. ID 2063 hosts an AGN, see text. Dark green triangles – confirmed non-members. Purple triangles – targets for which the spectra do not allow redshift determination. Green diamonds – blue stars included in the mask to facilitate correction for telluric absorption lines. Red star – the brightest cluster galaxy (BCG), not part of our spectroscopic sample as it has a triple core, see text. The approximate location of two *HST/ACS* fields are marked with black lines.

Table 3 gives an overview of the obtained spectroscopic observations, while Table 4 summarizes the instrument parameters for the observations. After the initial observations from program GN-2011B-DD-5 non-members identified from those observations were eliminated in the mask made for program GN-2013A-Q-65 and other potential members were included instead using the same selection criteria as used for the original mask.

The spectroscopic observations were processed using the methods described in detail in Jørgensen & Chiboucas (2013). The only exception was the handling of the charge diffusion

effect, which for the E2V DD CCDs turns out to have a spatial dependence in addition to variation with wavelength. The adopted correction is described in the Appendix.

The data processing results in 1-dimensional spectra calibrated to a relative flux scale. The spectra were used to derive redshifts, and for those targets with sufficient S/N, velocity dispersions and absorption line strengths. The spectroscopic parameters were determined using the same methods as described in Jørgensen et al. (2005). In particular, the redshifts and velocity dispersions were determined by fitting the spectra with a mix of three template stars (spectral types K0III,

Table 1
GMOS-N Observations

Cluster	Program ID	Dates [UT]	Data type	Program type
RXJ0848.6+4445	GN-2011B-DD-3 ^a	UT 2011 October 1 to 2011 October 2	imaging	DD in queue ^c
	GN-2011B-DD-3 ^b	UT 2011 December 6	imaging	DD in queue ^c
	GN-2011B-DD-5	UT 2011 November 24 to 2012 January 4	spectroscopy	DD in queue ^c
	GN-2013A-Q-65	UT 2013 March 9 to 2013 May 18	spectroscopy	queue

^a Observations obtained with the original E2V CCDs.

^b Observations obtained with the E2V DD CCDs.

^c Director's Discretionary time.

Table 2
HST/ACS Imaging Data

Cluster	No. of fields	Filter	Total t_{exp} (s)	Program ID
RXJ0848.6+4453 F1	6	F775W	7300	9919
RXJ0848.6+4453 F2	6	F775W	7300	9919
RXJ0848.6+4443 F1	10	F850LP	12220	9919
RXJ0848.6+4443 F2	10	F850LP	12220	9919

Table 3
GMOS-N Spectroscopic Data

Cluster	Program ID	Exposure time	N_{exp} ^a	FWHM ^b (arcsec)	σ_{inst} ^c	Aperture ^d (arcsec)	Slit lengths (arcsec)	S/N ^e
RXJ0848.6+4453	GN-2011B-DD-5	39,600 sec	22	0.56	...	1 × 0.7, 0.53	2.75	
	GN-2013A-Q-65	43,200 sec	24	0.58	...	1 × 0.7, 0.53	2.75	
	combined	82,800 sec	46	0.57	3.013Å, 100 km s ⁻¹	1 × 0.7, 0.53	2.75	13.3

^a Number of individual exposures.

^b Image quality measured as the average FWHM at 8000Å of the blue stars included in the masks.

^c Median instrumental resolution derived as sigma in Gaussian fits to the sky lines of the stacked spectra. The second entry is the equivalent resolution in km s⁻¹ at 4000Å in the rest frame of the cluster.

^d The first entry is the rectangular extraction aperture (slit width × extraction length). The second entry is the radius in an equivalent circular aperture, $r_{ap} = 1.025(\text{length} \times \text{width}/\pi)^{1/2}$, cf. Jørgensen et al. (1995b).

^e Median S/N per Ångstrom for the 24 cluster members, in the rest frame of the cluster.

Table 4
Gemini North Instrumentation for Spectroscopic Observations

Instrument	GMOS-N
CCDs	3 × E2V DD 2048 × 4608
r.o.n. ^a	(3.17, 3.22, 3.46) e ⁻
gain ^a	(2.31, 2.27, 2.17) e ⁻ /ADU
Pixel scale	0.0727 arcsec/pixel
Field of view	5'5 × 5'5
Grating	R400_G5305
Spectroscopic filter	OG515_G0306
Wavelength range ^b	5500-10500Å

^a Values for the three detectors in the array.

^b The exact wavelength range varies from slitlet to slitlet.

G1V, and B8V) using software made available by Karl Gebhardt (Gebhardt et al. 2000, 2003). The galaxies that were found to be members of the cluster were fit in the wavelength range 3750–4100Å. Table 11 in the Appendix gives the results from the template fitting. The velocity dispersions were aperture corrected using the technique from Jørgensen et al. (1995b). Of the 52 targets observed, 24 turned out to be members of the cluster. Of these 19 have velocity dispersion deter-

mined. The median S/N of these is 18 per Ångstrom in the rest frame (see Table 11 for the S/N of the individual spectra). Velocity dispersions were determined for 10 non-members, see Table 11. We assessed the possible systematic errors on the derived velocity dispersions resulting from the determination of the instrumental resolution, the adopted telluric correction, and the sky subtraction. None of these sources cause systematic errors that affect our results significantly, see Appendix for details.

The spectra allow determination of following absorption line indices: CN3883, CaHK, D4000, and H ζ_A . The indices CN3883 and CaHK are defined in Davidge & Clark (1994). For D4000 we use a shorter red passband than usually used (Gorgas et al. 1999) but calibrate our measurements to be consistent with the conventional definition of the index, see Appendix for details. For the high order Balmer line index H ζ_A we adopt the definition from Nantais et al. (2013). All measured indices are listed in Table 12 in the Appendix.

For galaxies with detectable [O II] emission the strength of the emission line was determined both as a (relative) flux and as an equivalent width (Table 12). Due to the very weak continuum of some of the emission line galaxies, the equivalent widths in some cases have very large uncertainties.

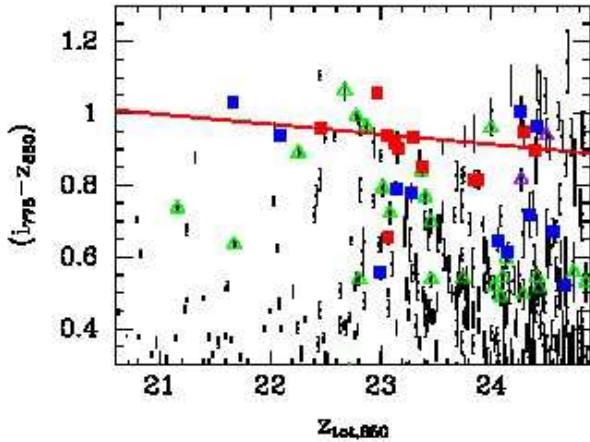


Figure 2. Color-magnitude relation of galaxies in the RXJ0848.6+4453 field. Red squares – members of the cluster with $\text{EW}[\text{O II}] \leq 5 \text{ \AA}$; blue squares – members with $\text{EW}[\text{O II}] > 5 \text{ \AA}$; green open triangles – confirmed non-members; purple open triangles – galaxies for which the obtained spectra do not allow redshift determination; small black points – all galaxies in the field. Red line is the best fit to the 16 member galaxies with $(i_{775} - z_{850}) \geq 0.8$: $(i_{775} - z_{850}) = 0.969 - (0.028 \pm 0.024)(z_{\text{tot},850} - 22.5)$ with $\text{rms} = 0.073$.

The $[\text{O II}]$ emission makes it possible to determine the star formation rates (SFR), under the assumption that the line is due to star formation only. We have examined the spectra for the presence of the two neon lines $[\text{Ne V}]3426 \text{ \AA}$ and $[\text{Ne III}]3869 \text{ \AA}$. The line $[\text{Ne V}]3346 \text{ \AA}$ is at the cluster redshift too close to strong telluric absorption to be reliably detected. These are the only strong lines originating from active galactic nuclei (AGNs) that are in the covered wavelength region (e.g., Schmidt et al. 1998; Mignoli et al. 2013). Only ID 2063 have detectable Ne emission. We proceed to determine the SFR from the $[\text{O II}]$ line and flag ID 2063 in the relevant figures in the analysis of the data.

2.3. Data for other clusters

In the analysis we use our data for the $z = 0.5 - 0.9$ clusters published in our previous papers (Jørgensen et al. 2005; Chiboucas et al. 2009; Jørgensen & Chiboucas 2013). These papers present ground-based spectroscopy and *HST*/ACS imaging of MS0451.6–0305 ($z = 0.54$), RXJ0152.7–1357 ($z = 0.83$), and RXJ1226.9+3332 ($z = 0.89$). Further, we use our data for Coma, Perseus and Abell 194, (Jørgensen et al. 1995ab, 1999; Jørgensen & Chiboucas 2013), as our $z \approx 0$ comparison sample. Table 5 summarizes the cluster properties for all the clusters. The samples in all clusters are selected consistently. Except for MS0451.6–0305, the passbands used for the determination of the effective parameters correspond roughly to rest frame B-band, as is the case for the RXJ0848.6+4453 observations presented in this paper. MS0451.6–0305 was observed in F814W, which at $z = 0.54$ is close to rest frame V-band. Thus, if the color gradients the MS0451.6–0305 galaxies are similar to those in nearby early-type galaxies, typically $\Delta(B-V)/\Delta \log r \approx -0.04$ (e.g., Saglia et al. 2000), then the effective radii derived from F814W can be expected to be about 6% smaller than if derived from a passband matching rest frame B-band for the cluster (Sparks & Jørgensen 1993).

3. CLUSTER REDSHIFT, VELOCITY DISPERSION, SUBSTRUCTURE, AND CLUSTER MASS

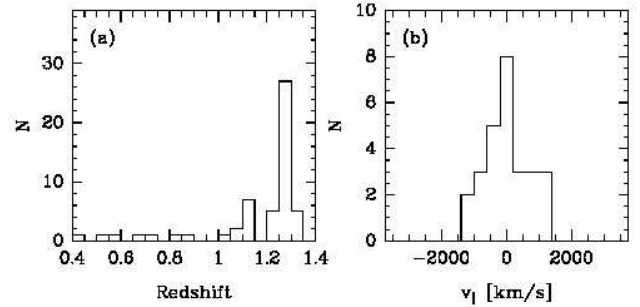


Figure 3. (a) Redshift distribution of the spectroscopic sample. (b) Distribution of the radial velocities (in the rest frame of the cluster) relative to the cluster redshifts for cluster members, $v_{||} = c(z - z_{\text{cluster}})/(1 + z_{\text{cluster}})$. The radial velocity distributions for the members are not significantly different from a Gaussian distribution.

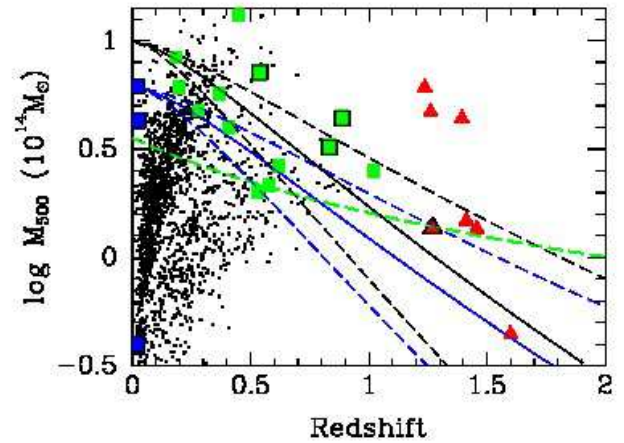


Figure 4. The cluster masses, M_{500} , based on X-ray data versus the redshifts of the clusters. Blue – our low redshift comparison sample (Coma, Perseus, A194); green – our main $z = 0.2 - 1$ cluster sample, MS0451–0305, RXJ0152.7–1357, and RXJ1226.9+3332 shown with black outlines; M_{500} from Piffaretti et al. (2011). Red – our current sample of $z = 1.2 - 1.6$ clusters, RXJ0848.6+4453/Lynx W shown with black outline. The $z = 1.2 - 1.6$ clusters and references for the cluster masses are: RDCS J1252.9–2927 (Stott et al. 2010), RXJ0848.6+4453/Lynx W (Ettori et al. 2004), RXJ0848.9+4452/Lynx E (Stott et al. 2010), XMM2235.3–2557 (Rosati et al. 2009), J1438.1+3414 (Brodwin et al. 2011), J2215.0–1738.1 (Stott et al. 2010), J0332–2742 (M_{500} derived from L_{500} in Kurk et al. 2009, using approximation from Vikhlinin et al. 2009). Small black points – all clusters from Piffaretti et al. shown for reference. Green line – original X-ray luminosity limit for our $z = 0.2 - 1$ cluster sample (Jørgensen & Chiboucas 2013). Blue and black lines – mass development of clusters based on numerical simulations by van den Bosch (2002). The black lines terminate at $\text{Mass} = 10^{15} M_{\odot}$ at $z = 0$ roughly matching the highest mass clusters at $z = 0.1 - 0.2$. The blue lines terminate at $\text{Mass} = 10^{14.8} M_{\odot}$ at $z = 0$ matching the mass of the Perseus cluster. The dashed lines represent the typical uncertainty in the mass development represented by the numerical simulations.

We determined the cluster redshift and velocity dispersion using the bi-weight method (Beers et al. 1990). Figure 3 shows the redshift distribution of the sample. We find a redshift of 1.2701 ± 0.0010 and a cluster velocity dispersion of $733_{-85}^{+84} \text{ km s}^{-1}$. Galaxies with redshifts in the interval $z = 1.26 - 1.28$ are considered members of the cluster, see Table 11 in the Appendix for membership information of the individual galaxies.

Using a Kolmogorov-Smirnov test, we tested whether the velocity distribution of the member galaxies deviate from a Gaussian. The probability of the sample being drawn from a Gaussian distribution is 99%. Thus, we conclude that no

Table 5
Cluster Properties

Cluster	Redshift	σ_{cluster} km s ⁻¹	L_{500} 10 ⁴⁴ erg s ⁻¹	M_{500} 10 ¹⁴ M_{\odot}	R_{500} Mpc	N_{member}
(1)	(2)	(3)	(4)	(5)	(6)	(7)
Perseus = Abell 426 ^a	0.0179	1277 ⁺⁹⁵ ₋₇₈	6.217	6.151	1.286	63
Abell 194 ^{a,b}	0.0180	480 ⁺⁴⁸ ₋₃₈	0.070	0.398	0.516	17
Coma = Abell 1656 ^d	0.0231	1010 ⁺⁵¹ ₋₄₄	3.456	4.285	1.138	116
MS0451.6–0305 ^c	0.5398 ± 0.0010	1450 ⁺¹⁰⁵ ₋₁₅₉	15.352	7.134	1.118	47
RXJ0152.7–1357 ^d	0.8350 ± 0.0012	1110 ⁺¹⁴⁷ ₋₁₂₂	6.291	3.222	0.763	29
RXJ1226.9+3332 ^c	0.8908 ± 0.0011	1298 ⁺¹⁷⁴ ₋₁₃₇	11.253	4.386	0.827	55
RXJ0848.6+4443 ^e	1.2701 ± 0.0010	733 ⁺⁸⁴ ₋₈₅	1.04	1.37	0.499	24

Note. — Col. (1) Galaxy cluster; col. (2) cluster redshift; col. (3) cluster velocity dispersion; col. (4) X-ray luminosity in the 0.1–2.4 keV band within the radius R_{500} , from Piffaretti et al. (2011), except for RXJ0848.6+4443 for which the data are from Ettori et al. (2004); col. (5) cluster mass derived from X-ray data within the radius R_{500} , from Piffaretti et al., except for RXJ0848.6+4443 for which the data are from Ettori et al.; col. (6) radius within which the mean over-density of the cluster is 500 times the critical density at the cluster redshift, from Piffaretti et al., except for RXJ0848.6+4443 for which the data are from Ettori et al.; col. (7) Number of member galaxies for which spectroscopy is used in this paper.

^a Redshift and velocity dispersion from Zabludoff et al. (1990).

^b Abell 194 does not meet the X-ray luminosity selection criteria of the main cluster sample.

^c Redshifts and velocity dispersions from Jørgensen & Chiboucas (2013).

^d Redshift and velocity dispersion from Jørgensen et al. (2005). The velocity dispersions for the Northern and Southern sub-clusters are (681 ± 232) km s⁻¹ and (866 ± 266) km s⁻¹, respectively.

^e Redshift and velocity dispersion from this paper.

Table 6
Predictions from Single Stellar Population Models

Relation (1)	rms (2)	Reference (3)
$\log M/L_B = 0.946 \log \text{age} + 0.333[M/H] - 0.063$	0.022	Maraston 2005
$\log H\zeta_A = -0.456 \log \text{age} - 0.462[M/H] + 0.563$	0.049	Maraston & Strömbäck 2011
CN3883 = 0.183 log age + 0.258[M/H] + 0.097	0.024	Maraston & Strömbäck 2011
D4000 = 0.617 log age + 0.807[M/H] + 1.695	0.069	Maraston & Strömbäck 2011
$\log \text{CaHK} = 0.086 \log \text{age} + 0.079[M/H] + 1.279$	0.011	Maraston & Strömbäck 2011

Note. — (1) Relation established from the published model values. $[M/H] \equiv \log Z/Z_{\odot}$ is the total metallicity relative to solar. The age is in Gyr. The M/L ratios are stellar M/L ratios in solar units. The models were fit for ages from 1 to 15 Gyr and $[M/H]$ from -0.3 to 0.3 . The relation for the M/L ratio differs slightly from the relation given in Jørgensen & Chiboucas (2013), as that paper did not include the 1 Gyr old models in the fit. (2) Scatter of the model values relative to the relation. (3) Reference for the model values.

sub-structure is detectable in the velocity distribution.

Table 5 summarizes the cluster properties for all clusters used in the analysis in this paper, including the X-ray luminosities, radii and masses from the literature. On Figure 4 we show the cluster masses versus redshifts for these clusters. For reference the figure also shows our full cluster sample and the catalog of $z < 1$ clusters from Piffaretti et al. (2011). We show sample models for the growth of cluster masses with time, based on results from van den Bosch (2002). These models are in general agreement with newer and more detailed analysis of the results from the Millennium simulations (Fakhouri et al. 2010). The mass of RXJ0848.9+4453 is significantly lower than the other clusters included in the present analysis. However, because of the expected growth of cluster masses with time, RXJ0848.9+4453 is a viable progenitor for clusters of masses similar to Coma and Perseus at $z \approx 0$.

We characterize the stellar populations in the RXJ0848.6+4453 galaxies by (1) establishing the FP, and the relations between masses, sizes and velocity dispersions; and (2) analyzing the absorption lines and SFR as function of galaxy velocity dispersion (or mass) and location within the cluster. In our analysis of the possible size and velocity dispersion evolution we present results using effective radii from both the fits with $r^{1/4}$ profiles and with Sérsic profiles. The results for the FP do not depend which of the two sets of effective parameters are used as on average the combination $\log r_e + \beta \log \langle I \rangle_e$ with $\beta = 0.66 - 0.82$ entering the FP varies less than 0.01 between the two choices of parameters. Further, since the low redshift comparison sample was fit with $r^{1/4}$ profiles we use the effective radii and surface brightnesses derived from the fits with $r^{1/4}$ profiles in our discussion of the FP.

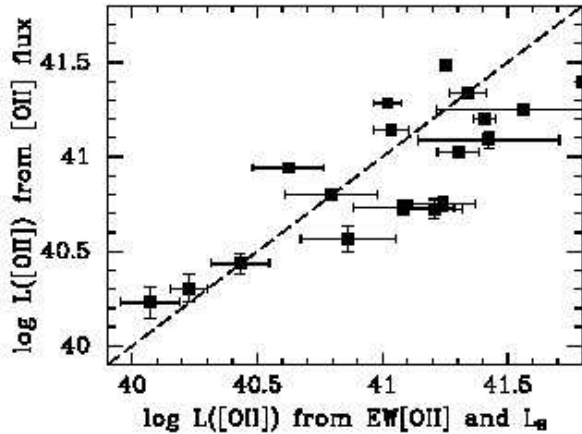


Figure 5. The luminosity of the [O II] emission, $L([\text{O II}])$, derived from $\text{EW}[\text{O II}]$ and L_B versus the luminosity derived directly from the [O II] flux. Dot-dashed line – one-to-one relation. Using the [O II] flux directly results in lower uncertainties on $L([\text{O II}])$. The offset of $\Delta \log L([\text{O II}]) = 0.1$ between the two methods is of no importance for our analysis. The offset due to a combination of the aperture size for the spectroscopy and the non-photometric conditions for some of those observations.

Our technique for establishing the scaling relations and associated uncertainties on slopes and zero points is the same as we used in Jørgensen et al. (2005) and Jørgensen & Chiboucas (2013). Briefly, we establish the scaling relations using a fitting technique that minimizes the sum of the absolute residuals perpendicular to the relation, determines the zero points as the median, and uncertainties on the slopes using a bootstrap method. The technique is very robust to the effect of outliers. The random uncertainties on the zero point differences, $\Delta\gamma$, between the intermediate redshift and low redshift samples are derived as

$$\sigma_{\Delta\gamma} = \left(\text{rms}_{\text{low-}z}^2 / N_{\text{low-}z} + \text{rms}_{\text{int-}z}^2 / N_{\text{int-}z} \right)^{0.5} \quad (1)$$

where subscripts “low- z ” and “int- z ” refer to the low redshift sample and one of the intermediate redshift clusters, respectively. In the presentation of the zero point differences we show only the random uncertainties. The systematic uncertainties on the zero point differences are expected to be dominated by the possible inconsistency in the calibration of the velocity dispersions, 0.026 in $\log \sigma$ (cf. Jørgensen et al. 2005), and may be estimated as 0.026 times the coefficient for $\log \sigma$, or 0.052 times the coefficient for $\log \text{Mass}$.

4.2. Single stellar population models

In the analysis we use spectral energy distributions (SED) for single stellar population (SSP) models to derive model values of the absorption line indices that we are able to determine from the spectra of RXJ0848.6+4453. We use the SEDs from Maraston & Strömbäck (2011) for a Salpeter (1955) initial mass function (IMF). In addition we use mass-to-light (M/L) ratios for very similar models from Maraston (2005).

As in Jørgensen & Chiboucas (2013) we have derived model relations linear in the logarithm of the age and in the metallicity $[\text{M}/\text{H}]$. These relations are listed in Table 6 and are used to aid our analysis. In the fits presented here we include the models with age 1 Gyr as our sample includes galaxies with very young stellar populations. The fits in Jørgensen & Chiboucas (2013) were derived excluding these very young models. Thus, the M/L ratio relation in Table 6 differs slightly

from the relation given by Jørgensen & Chiboucas.

The simplest models for the evolution of the stellar populations are passive evolution models. In such models it is assumed that after an initial period of star formation the galaxies evolve passively without any additional star formation. The models are usually parameterized by a formation redshift z_{form} , which corresponds to the approximate epoch of the last major star formation episode. In these models the age difference between galaxies at different redshifts is expected to be equal to the difference in lookback time. Thus, the relations listed in Table 6 enable us for a given z_{form} to derive the expected offsets for the M/L ratios and the line indices between the high redshift clusters and our $z \approx 0$ comparison sample. Alternatively, we can derive a formation redshift z_{form} from the measured offsets of the parameters.

The formation redshift may depend on the galaxy properties and/or the properties of the cluster environment (e.g. Thomas et al. 2005). In our analysis we use the model from Thomas et al. for the high density environment, which prescribes a formation redshift z_{form} dependent on the velocity dispersion of the galaxy. We convert the velocity dispersion dependency to a mass dependency using an empirical relation between dynamical mass and velocity dispersion (see Jørgensen & Chiboucas 2013).

In our analysis, we implicitly assume that the galaxies we observe in RXJ0848.6+4453 can be considered progenitors to the galaxies in the clusters at lower redshifts. As discussed in detail by van Dokkum & Franx (2001) this may not be a valid assumption. We return to this issue in the discussion (Sect. 6).

4.3. Dynamical masses

The dynamical masses of the galaxies can be determined from the velocity dispersions and effective radii as $\text{Mass} = \beta r_e \sigma^2 G^{-1}$, with $\beta = 5$ (Bender et al. 1992). Cappellari et al. (2006) found from integral-field-unit (IFU) data that this approximation provides a reasonable mass estimate in the absence of observational data like IFU data, which would enable more detailed modeling. These authors also tested the use of a coefficient β dependent on the Sérsic index n_{ser} . They derived an expression based on a spherical isotropic model

$$\beta(n_{\text{ser}}) = 8.87 - 0.831 n_{\text{ser}} + 0.0241 n_{\text{ser}}^2 \quad (2)$$

Their conclusion is that this expression does not improve the mass estimate over using $\beta = 5$, when comparing to the masses derived from their full modeling. Alternatively, van Dokkum et al. (2010) derived a fit to the numerical results from Ciotti (1991) and suggested the expression

$$\beta(n_{\text{ser}}) = 3.316 + 0.026 n_{\text{ser}} - 0.035 n_{\text{ser}}^2 + 0.00172 n_{\text{ser}}^3 \quad (3)$$

We note that this expression does not reach $\beta = 5$ for any values of n_{ser} and therefore is not supported by the detailed modeling of IFU data done by Cappellari et al. (2006). In the following we adopt $\text{Mass} = 5 r_e \sigma^2 G^{-1}$ for the mass estimates.

4.4. Determination of the star formation rates

Traditionally determination of the SFR from the [O II] line has been done from the equivalent width, $\text{EW}[\text{O II}]$, using the calibrations from Kennicutt (1992) and Gallagher et al. (1989),

$$\text{SFR} = 1.4 \cdot 10^{-41} L([\text{O II}]) \quad (4)$$

Table 7
RXJ0848.6+4453 Sub-Samples

No.	Criteria	N	IDs	Notes
1	Only redshift & EW[O II] from spectra	5	654 1123 1533 1809 3426	ID 3426 has no significant [O II] emission
2	$n_{\text{ser}} < 1.5$, $\log \sigma$ meas.	4	1644 2349 2417 2772	IDs 1644 2349 2417 have $S/N < 10$
3	$n_{\text{ser}} \geq 1.5$, $\log \sigma$ meas., $S/N < 10$	2	2015 2702	ID 2015 has $\log \text{Mass} < 10.3$
4	$n_{\text{ser}} \geq 1.5$, $\log \sigma$ meas., $S/N \geq 10$, EW[O II] $> 5\text{\AA}$	5	807 1362 1763 1888 2063	$\log \text{Mass} \geq 10.3$, ID 2063 hosts an AGN
5	$n_{\text{ser}} \geq 1.5$, $\log \sigma$ meas., $S/N \geq 10$, EW[O II] $\leq 5\text{\AA}$	8	240 1264 1748 2111 2735 2943 2989 3090	$\log \text{Mass} \geq 10.3$

Table 8
Scaling Relations

Relation (1)	Low redshift			MS0451.6–0305			RXJ0152.7–1357			RXJ1226.9+3332			RXJ0848.6+4453		
	γ (2)	N_{gal} (3)	rms (4)	γ (5)	N_{gal} (6)	rms (7)	γ (8)	N_{gal} (9)	rms (10)	γ (11)	N_{gal} (12)	rms (13)	γ (14)	N_{gal} (15)	rms (16)
$\log r_e = (0.57 \pm 0.06) \log \text{Mass} + \gamma^a$	-5.734	105	0.16	-5.701	34	0.17	-5.682	21	0.11	-5.724	28	0.19	-5.806	8	0.22
$\log r_e = (0.57 \pm 0.06) \log \text{Mass} + \gamma^b$	-5.704	34	0.17	-5.715	21	0.10	-5.735	28	0.19	-5.843	8	0.27
$\log r_e = (0.57 \pm 0.06) \log \text{Mass} + \gamma^c$	-5.700	34	0.16	-5.713	21	0.10	-5.725	28	0.18	-5.838	8	0.27
$\log \sigma = (0.26 \pm 0.03) \log \text{Mass} + \gamma^a$	-0.667	105	0.08	-0.701	34	0.08	-0.716	21	0.05	-0.679	28	0.09	-0.635	8	0.10
$\log \sigma = (0.26 \pm 0.03) \log \text{Mass} + \gamma^b$	-0.694	34	0.08	-0.684	21	0.05	-0.673	28	0.09	-0.614	8	0.14
$\log \sigma = (0.26 \pm 0.03) \log \text{Mass} + \gamma^c$	-0.695	34	0.08	-0.686	21	0.05	-0.674	28	0.09	-0.617	8	0.14
$\log M/L = (0.24 \pm 0.03) \log \text{Mass} + \gamma$	-1.754	105	0.09	-2.144	34	0.15	-2.289	21	0.20	-2.410	28	0.19	-2.523	8	0.18
$\log M/L = (1.07 \pm 0.12) \log \sigma + \gamma$	-1.560	105	0.11	-1.974	34	0.13	-2.067	21	0.18	-2.197	28	0.17	-2.374	8	0.20
$\log H\zeta_A = (-0.76 \pm 0.29) \log \sigma + \gamma$	1.762	45	0.25	1.877	28	0.16	1.956	21	0.22	2.037	17	0.11	1.211	6	0.27
CN3883 = $(0.29 \pm 0.06) \log \sigma + \gamma$	-0.410	65	0.05	-0.410	31	0.03	-0.396	21	0.05	-0.400	23	0.04	-0.512	6	0.06
$\log \text{CaHK} = (0.14 \pm 0.04) \log \sigma + \gamma$	0.997	65	0.05	1.030	31	0.03	1.019	21	0.05	1.028	22	0.02	0.986	6	0.12
D4000 = $(0.84 \pm 0.29) \log \sigma + \gamma$	0.209	65	0.19	0.123	31	0.11	0.166	21	0.20	0.149	26	0.11	0.171	7	0.20

Note. — (1) Scaling relation. (2) Zero point for the low redshift sample. (3) Number of galaxies included from the low redshift sample. (4) rms in the Y-direction of the scaling relation for the low redshift sample. (5), (6), and (7) Zero point, number of galaxies, rms in the Y-direction for the MS0451.6–0305 sample. (8), (9), and (10) Zero point, number of galaxies, rms in the Y-direction for the RXJ0152.7–1357 sample. (11), (12), and (13) Zero point, number of galaxies, rms in the Y-direction for the RXJ1226.9+3332 sample. (14), (15), and (16) Zero point, number of galaxies, rms in the Y-direction for the RXJ0848.6+4453 sample. Results for Low redshift sample, MS0451.6–0305, RXJ0152.7–1357, and RXJ1226.9+3332 for relations involving Mass, M/L and CN3883 are reproduced from Jørgensen & Chiboucas (2013). For the $\log \text{CaHK}$ relation the slope and zero points for the low redshift sample and RXJ0152.7–1357 are from Jørgensen et al. (2005).

^a Effective radii from fits with $r^{1/4}$ profiles, $r_e = (a_e b_e)^{1/2}$.

^b Effective radii from fits with Sérsic profiles, $r_e = (a_e b_e)^{1/2}$.

^c Effective radii from fits with Sérsic profiles, $r_e = (a_e + b_e)/2$.

Table 9
Fundamental Plane and Relations for the M/L Ratios

Cluster	Relation ^a	N_{gal}	rms
Coma	$\log r_e = (1.30 \pm 0.08) \log \sigma - (0.82 \pm 0.03) \log (I)_e - 0.443$	105	0.08
MS0451.6–0305	$\log r_e = (0.78 \pm 0.18) \log \sigma - (0.79 \pm 0.11) \log (I)_e + 0.983$	34	0.10
RXJ0152.7–1357, RXJ1226.9+3332 ^b	$\log r_e = (0.65 \pm 0.14) \log \sigma - (0.67 \pm 0.04) \log (I)_e + 1.070$	49	0.09
RXJ0152.7–1357, RXJ1226.9+3332, RXJ0848.6+4453 ^c	$\log r_e = (0.71 \pm 0.20) \log \sigma - (0.66 \pm 0.06) \log (I)_e + \{0.911, 0.901, 0.947\}$	57	0.09, 0.10, 0.10
Coma	$\log M/L = (0.24 \pm 0.03) \log \text{Mass} - 1.754$	105	0.09
MS0451.6–0305	$\log M/L = (0.44 \pm 0.09) \log \text{Mass} - 4.499$	34	0.14
RXJ0152.7–1357, RXJ1226.9+3332 ^b	$\log M/L = (0.55 \pm 0.08) \log \text{Mass} - 5.845$	49	0.14
RXJ0152.7–1357, RXJ1226.9+3332, RXJ0848.6+4453 ^c	$\log M/L = (0.55 \pm 0.06) \log \text{Mass} - \{5.849, 5.829, 5.911\}$	57	0.12, 0.12, 0.15
Coma	$\log M/L = (1.07 \pm 0.12) \log \sigma - 1.560$	105	0.11
MS0451.6–0305	$\log M/L = (1.47 \pm 0.29) \log \sigma - 2.894$	34	0.13
RXJ0152.7–1357, RXJ1226.9+3332 ^b	$\log M/L = (2.26 \pm 0.32) \log \sigma - 4.782$	49	0.17
RXJ0152.7–1357, RXJ1226.9+3332, RXJ0848.6+4453 ^c	$\log M/L = (2.16 \pm 0.0.27) \log \sigma - \{4.542, 4.593, 4.902\}$	57	0.12, 0.18, 0.29

^a The fits for Coma, MS0451.6–0305, RXJ0152.7–1357 and RXJ1226.9+3332 are adopted from Jørgensen & Chiboucas (2013) and listed here for completeness.

^b RXJ0152.7–1357 and RXJ1226.9+3332 treated as one sample.

^c RXJ0152.7–1357, RXJ1226.9+3332, and RXJ0848.6+4453 fit with parallel relations. The zero points and rms for the three samples are listed in the same order as the clusters.

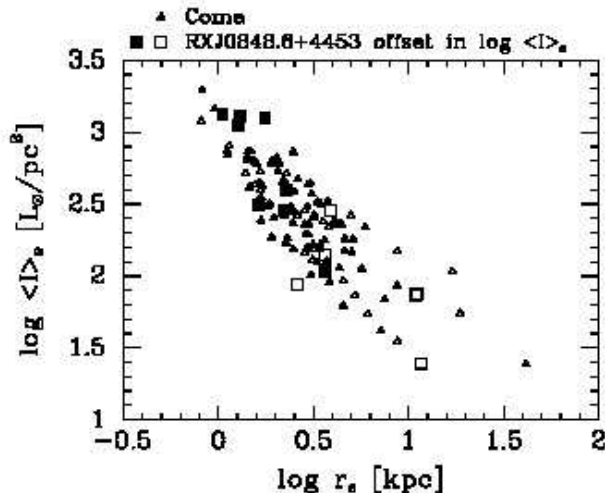


Figure 6. Effective radii versus mean surface brightnesses for the Coma cluster sample and the RXJ0848.6+4453 sample. Open triangles – Coma cluster; solid boxes – bulge-dominated members of RXJ0848.6+4453 with $\text{EW}[\text{O II}] \leq 5 \text{ \AA}$ (sample 5); open boxes – bulge-dominated members of RXJ0848.6+4453 with $\text{EW}[\text{O II}] > 5 \text{ \AA}$ (sample 4). The data for the RXJ0848.6+4453 sample have been offset with -0.769 in $\log \langle I \rangle_e$ to take into account the luminosity offset relative to the Coma cluster. After applying this offset, the distribution in the $\log r_e - \log \langle I \rangle_e$ space of the RXJ0848.6+4453 sample is similar to that of the Coma cluster sample.

with the SFR in $M_\odot \text{ yr}^{-1}$ and the $[\text{O II}]$ luminosity $L([\text{O II}])$ in erg sec^{-1} derived from the equivalent width $\text{EW}[\text{O II}]$ as

$$L([\text{O II}]) = 1.4 \cdot 10^{29} L_B \text{EW}([\text{O II}]) \quad (5)$$

where L_B is the luminosity of the galaxy in rest frame B-band in solar units.

Due to the very faint continuum of most of the star forming galaxies in our sample, the uncertainty on $\text{EW}[\text{O II}]$ is dominated by the uncertainty on the continuum level and are typically 20-25%, while the direct measurement of the relative $[\text{O II}]$ flux is accurate to 8-10%. Thus, rather than use $\text{EW}[\text{O II}]$ and L_B to derive SFR, we instead opt to use the $[\text{O II}]$ flux directly. One could argue that because of the limited size spectral aperture and the possible non-photometric conditions during some of the spectroscopic observations that we therefore underestimate the total $[\text{O II}]$ flux. To evaluate the size of this effect we derived $L[\text{O II}]$ both from $\text{EW}[\text{O II}]$ and L_B and directly from the $[\text{O II}]$ flux. The $[\text{O II}]$ flux was converted to $L[\text{O II}]$ using a luminosity distance of $D_L = 8880.3 \text{ Mpc}$, which corresponds to $z = 1.27$ for our adopted cosmology. The $L[\text{O II}]$ values from the two methods are compared on Figure 5. The median offset between the two values is $\Delta \log L[\text{O II}] = 0.1$. Thus, using the $[\text{O II}]$ flux leads to the SFR being underestimated with a similar amount. However, this small offset is of no importance for our analysis, and since the uncertainties on $L[\text{O II}]$ are about half of those for $L[\text{O II}]$ based on the $\text{EW}[\text{O II}]$ we have used Equation 4 to derive the SFR.

4.5. Sub-samples in RXJ0848.6+4453

In Table 7 we divide the 24 members in sub-samples according to available spectroscopic parameters, S/N, Sérsic index and the strength of the $[\text{O II}]$ emission. Our main sample consists of sub-samples (4) and (5), which are the bulge-dominated galaxies with $\text{EW}[\text{O II}] > 5 \text{ \AA}$ and $\leq 5 \text{ \AA}$, respectively.

For the analysis of the FP and the relations between masses, sizes and velocity dispersions we concentrate on sample (5), the bulge-dominated galaxies with $\text{EW}[\text{O II}] \leq 5 \text{ \AA}$. Except for allowing galaxies with lower S/N spectra as part of the analysis, the selection criteria for sample (5) are the same as used in Jørgensen & Chiboucas (2013) as we will use the results presented in that paper as part of our analysis. We show the bulge-dominated galaxies with $\text{EW}[\text{O II}] > 5 \text{ \AA}$ (sample 4) on the figures, but they are excluded from the determination of the zero points for the relations. In the discussion of the absorption line strengths we show samples (4) and (5), as well as the four disk-dominated galaxies from sample (2) on the figures. We also show the disk-dominated galaxies from the $z < 1$ clusters. However, the relations as well as zero points are derived from the bulge-dominated galaxies with $\text{EW}[\text{O II}] \leq 5 \text{ \AA}$, only (sample 5 in RXJ0848.6+4453). In the discussion of the star formation rates derived from the $[\text{O II}]$ emission all cluster members are included.

Before we proceed, we briefly assess possible selection effects in our RXJ0848.6+4453 sample. We first note that our sample covers galaxies with effective radii $r_e \geq 1 \text{ kpc}$. This lower limit is similar to other studies of galaxies at $z \approx 1$, in particular the study by Saglia et al. (2010), with which we will compare in our analysis of the data. Within the two *HST*/ACS fields of RXJ0848.6+4453 there are 33 galaxies with $z_{850} \leq 24.5$ and within 0.1 mag of the CM relation. We have obtained spectroscopy of 20 of these. The magnitude distribution of the spectroscopically observed galaxies is not significantly different from that of all 33 galaxies as tested with Kolmogorov-Smirnov test. It is beyond the scope of this paper to determine effective radii and surface brightnesses of all the galaxies not included in the spectroscopic sample. However, the bulge-dominated members, (samples 4) and (5) included in the analysis are distributed in the $\log r_e - \log \langle I \rangle_e$ space similarly to our Coma cluster sample, when the luminosity evolution of -0.769 in $\log \langle I \rangle_e$ is taken into account, see Figure 6. We emphasize that the purpose of this figure is *not* to determine the luminosity offset for RXJ0848.6+4453 relative to the Coma cluster from this projection of the FP, but only to assess the distributions in $\log r_e$ and $\log \langle I \rangle_e$. In conclusion, there are no obvious selection effects related to sizes, luminosities or surface brightnesses that may bias our results as presented in the following.

5. SCALING RELATIONS, STELLAR POPULATIONS AND STAR FORMATION

The main results are described in the following subsections. Section 5.1 focuses on our results regarding the possible size and velocity dispersion evolution of the galaxies in RXJ0848.6+4453. Section 5.2 concentrates on the FP for the cluster, while the results regarding the stellar populations based on measurements of absorption and emission lines are outlined in Section 5.3.

The established scaling relations are summarized in Tables 8 and 9, and shown on Figures 7, 8, 9, and 10.

5.1. Radii and velocity dispersions as a function of masses

Figure 7 shows the effective radii and velocity dispersions versus the dynamical masses. The figure shows our data for RXJ0848.6+4453 together with our data for the $z = 0.5 - 0.9$ clusters and the Coma cluster sample for effective radii derived from fits with $r^{1/4}$ profiles, panels (a) and (b). In panels (c)-(d) and (e)-(f) we show RXJ0848.6+4453 together with

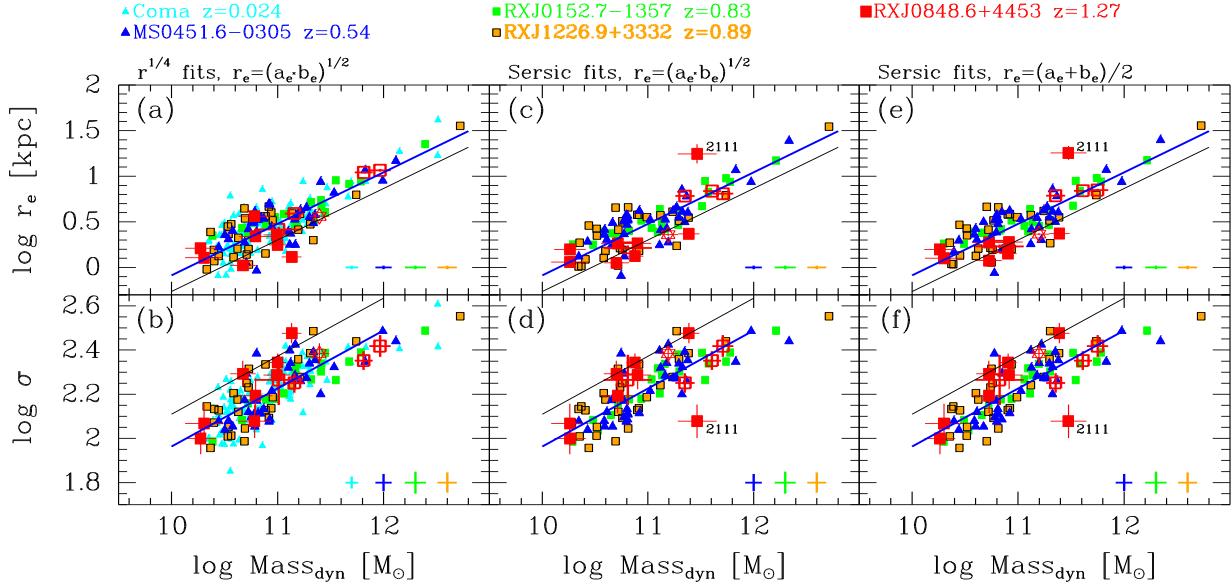


Figure 7. Effective radii and velocity dispersions versus dynamical masses. Panels (a) and (b) use effective radii from fits with $r^{1/4}$ profiles, $r_e = (a_e b_e)^{1/2}$. Panels (c) and (d) use effective radii from fits with Sérsic profiles, $r_e = (a_e b_e)^{1/2}$. Panels (e) and (f) use effective radii from fits with Sérsic profiles, $r_e = (a_e + b_e)/2$. Sérsic profile parameters are not available for the Coma cluster galaxies. Cyan – Coma cluster members; blue – MS0451.6-0305; green – RXJ0152.7-1357; orange – RXJ1226.9+3332; red – RXJ0848.6+4453. Open symbols for RXJ0848.6+4453 – galaxies with $\text{EW}[\text{O II}] > 5\text{\AA}$. Star – ID 2063, which hosts an AGN. Blue lines – best fit relations to the Coma cluster galaxies using effective radii from fits with $r^{1/4}$ profiles. The three clusters at $z < 1$ follow the same relation (Jørgensen & Chiboucas 2013). Black lines – predicted location of the RXJ0848.6+4453 galaxies under the assumption that the evolution found by Saglia et al. (2010) is valid for these galaxies. ID 2111 (marked) has a best fit Sérsic parameter of $n_{\text{ser}} = 9.1$ causing the significantly different position in panels (c)-(f) relative to panels (a) and (b).

the $z = 0.5 - 0.9$ clusters using Sérsic effective radii derived as $r_e = (a_e b_e)^{1/2}$ and $r_e = (a_e + b_e)/2$, respectively. On all the panels in Figure 7 the fit for the Coma cluster sample is shown (blue lines) together with the prediction of the location of the RXJ0848.6+4453 sample based on the results from Saglia et al. (2010) for dynamical masses (black lines). Table 8 summarizes the zero points for the relations for all the clusters. For RXJ0848.6+4453 the zero points are derived from the eight bulge-dominated galaxies with $\text{EW}[\text{O II}] \leq 5\text{\AA}$ (sample 5, see Table 7).

As described in Jørgensen & Chiboucas (2013), we found no significant evolution in effective radii or velocity dispersions at a given mass with redshift for the $z = 0.5 - 0.9$ clusters. In that paper we used effective radii from $r^{1/4}$ profiles. As the only cluster in the sample MS0451.6-0305 was observed in a passband matching roughly rest frame V, rather than rest frame B. Due to color gradients this is expected to result in $\log r_e$ on average being 0.028 smaller than if measured from a passband matching rest frame B (cf., Section 2.3). As the dynamical mass also depends on the effective radius, correcting for this effect would change the zero point for the size-mass relations for the cluster with an insignificant amount of -0.012 .

Using the $r^{1/4}$ effective radii, the offsets for the RXJ0848.6+4453 sub-sample of bulge-dominated $\text{EW}[\text{O II}] \leq 5\text{\AA}$ galaxies relative to the Coma cluster relations is about a third of what is expected based on the results from Saglia et al. Further, the offsets are significant only at the 1-sigma level. If we use the effective radii from the Sérsic profiles the offsets relative to the $z = 0.5 - 0.9$ clusters are slightly larger, though still only significant at the 1-1.5 sigma level. We note that Saglia et al. used effective radii derived as $r_e = (a_e + b_e)/2$. However, we find no significant

difference between using $r_e = (a_e b_e)^{1/2}$ and $r_e = (a_e + b_e)/2$ for our samples.

Concentrating on the results based on the $r^{1/4}$ effective radii, we convert the the median offsets in radii and velocity dispersions to an estimate of the median change of the dynamical mass, using $\text{Mass} = 5r_e \sigma^2 G^{-1}$. This indicates in an insignificant mass change, $\Delta \log \text{Mass} = 0.01 \pm 0.11$. Taking the uncertainty into account we can interpret this as an upper limit on the mass increase of ≈ 23 percent.

The five bulge-dominated emission line galaxies (sample 4 in Table 7) show no offsets in effective radii or velocity dispersion relative to the Coma cluster relations (Fig. 7) when using $r^{1/4}$ effective radii and also no offsets relative to the $z = 0.5 - 0.9$ clusters when using the effective radii based on Sérsic profiles.

5.2. The Fundamental Plane and relations for the M/L ratios

Figure 8 shows the FP edge-on for the RXJ0848.6+4453 samples (4) and (5) (Table 7) together with our samples for $z = 0.5 - 0.9$ clusters and the Coma cluster samples. On Figure 9 we show the FP as the M/L ratios versus the dynamical masses and versus the velocity dispersions. Tables 8 and 9 summarize the derived relations and zero points. All results in these two tables relating to only the $z = 0.5 - 0.9$ clusters and the Coma cluster samples are adopted from Jørgensen & Chiboucas (2013) and reproduced here to aid the discussion of the results for the RXJ0848.6+4453 sample.

The RXJ0848.6+4453 sample appears to follow a steep relation in M/L versus Mass and M/L versus velocity dispersion, as is the case for the two highest redshift clusters RXJ0152.7-1357 and RXJ1226.9+3332 from Jørgensen & Chiboucas. However, because the sample contains only eight galaxies it is not possible to determine the slopes of the re-

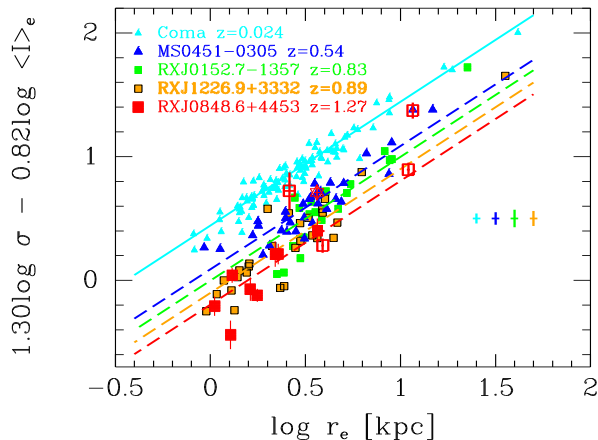


Figure 8. The Fundamental Plane shown edge-on. Symbols as on Fig. 7. Cyan line – best fit relation for the Coma cluster sample. Dashed lines – the Coma cluster FP offset to the median zero point for each of the four higher redshift clusters. The color coding of the lines match the symbols (blue – MS0451–0305; green – RXJ0152.7–1357; orange – RXJ1226.9+3332; red – RXJ0848.6+4453).

lations or the coefficients in the FP by fitting only this sample. Instead we have determined the best fit relations by fitting parallel relations to the three clusters. Thus, the assumption is that only the zero point varies between these clusters. Table 9 summarizes the derived relations. As the zero points for RXJ0152.7–1357 and RXJ1226.9+3332 are not significantly different from each other (cf. Jørgensen & Chiboucas 2013) we use their common zero point. We then derive the zero point difference for RXJ0848.6+4453 relative to that, and from there derive the formation redshift z_{form} required for the galaxies in RXJ0848.6+4453 to evolve passively to the location of the M/L versus Mass relation for RXJ0152.7–1357 and RXJ1226.9+3332. However, the zero point difference is so small that $z_{\text{form}} = \infty$ is needed. Thus, we conclude that the location of the M/L versus Mass relation for RXJ0152.7–1357 and RXJ1226.9+3332 cannot be the result of passive evolution of a higher redshift sample like the RXJ0848.6+4453 sample.

The zero point offset for RXJ0848.6+4453 (sample 5) relative to the Coma cluster sample is consistent with passive evolution and a formation redshift of $z_{\text{form}} = 1.95^{+0.22}_{-0.15}$. All eight galaxies in this sample have $\log \text{Mass} < 11.1$. The higher mass galaxies in the cluster have stronger emission lines and show a much larger scatter around the M/L versus Mass relation. We note that the $z = 0.5 - 0.9$ clusters contain low mass galaxies with z_{form} significantly below 1.95. We return to the discussion of this in Section 6.

5.3. Stellar populations: Absorption and emission lines

In Figure 10 we show the available absorption line indices versus the velocity dispersions. The figure includes the disk-dominated galaxies from all the clusters. For RXJ0848.6+4453 these are the galaxies listed in Table 7 as sample (2). Table 8 lists the relations shown on the figure. The correlation between the $H\zeta_A$ indices and the velocity dispersions is only significant for the sample of galaxies in MS0451.6–0305, for which a Kendall’s τ rank order test gives a probability of 0.7% of no correlation being present. For all the other cluster samples, the probabilities are 22% or larger that there is no correlation. We have therefore established the

slope of the relation fitting only the MS0451.6–0305 sample. For this relation the residuals were minimized in the direction of $H\zeta_A$. The zero points for all the samples were then derived using the slope established from the MS0451.6–0305 sample.

The correlation between the D4000 indices and the velocity dispersions for the individual clusters is weak. However, a Kendall’s τ rank order test for the joint sample of all the galaxies in the $z < 1$ samples yields a probability of 0.4% of no correlation being present. Thus, we determine the slope by fitting the full sample. After this, we determine the cluster specific zero points relative to this relation.

The main results we derive from Figure 10 and the relations in Table 8 are (1) the presence of very strong $H\zeta$ lines in the RXJ0848.6+4453 galaxies compared to the lower redshift samples, (2) the RXJ0848.6+4453 galaxies have significantly weaker CN3883 than found for the lower redshift samples, and (3) the RXJ0848.6+4453 galaxies are not significant offset in D4000 or CaHK relative to the lower redshift samples, though the scatter in these indices may be somewhat larger than for the lower redshift samples. It should be noted that except for CN3883 being weaker in the RXJ0848.6+4453 galaxies than in the lower redshift samples, none of the offsets in D4000, CaHK and CN3883 between the $z = 0.5 - 1.3$ clusters and the low redshift comparison sample are significant. We return to this in the discussion in Section 6.

We then investigate whether it is possible to use a combination of indices to estimate ages and metallicities of the galaxies in RXJ0848.6+4453. Figure 11 shows the strength of $H\zeta_A$ versus CN3883, CaHK, and D4000. The figure also shows model predictions based on the SSP SEDs from Maraston & Strömbäck (2011). These predictions are degenerate in metallicity and age. Thus, we can only approximately estimate the ages of the stellar populations from the indices. The metallicities cannot be constrained beyond noting that due to the strength of CaHK and CN3883 the metallicities of the RXJ0848.6+4453 galaxies must be similar to those of the lower redshift galaxies, i.e. solar or above solar. The best age estimates come from using $H\zeta_A$ versus CN3883. The area in this diagram populated by the RXJ0848.6+4453 galaxies (see Fig. 11a) can only be reached if the stellar population ages are 1–2 Gyr. Only a handful of the $z = 0.5 - 0.9$ bulge-dominated galaxies populate the same part of the diagram.

Figure 12 shows the star formation rates derived from the [O II] emission as well as the strength of the $H\zeta$ line versus the cluster center distance, R_{cluster} , and versus the dynamical mass. As not all galaxies have determination of the dynamical mass, Figure 12b contains fewer points than Figure 12a. Figures 12c and d show only galaxies with measurements of $H\zeta_A$, which in particular excludes the three low mass ($\text{Mass} < 10^{10.5} M_{\odot}$) galaxies that are included on Figure 12b. From Figures 12a and c we conclude that star forming galaxies and galaxies with strong $H\zeta_A$ are present throughout the cluster. There is no trend in SFR or $H\zeta_A$ with R_{cluster} , and also no radius within which star formation is absent. Figures 12b and d show that star formation and strong $H\zeta_A$ are present in the most massive of the bulge-dominated galaxies. However, the SFR is well below that of galaxies on the star formation “main sequence” (e.g., Wuyts et al. 2011).

6. DISCUSSION

In this discussion, we compare the results regarding the size and velocity dispersion evolution to previous results and discuss the possible effect of the cluster environment on this evolution. We then discuss the evolution in the stellar population

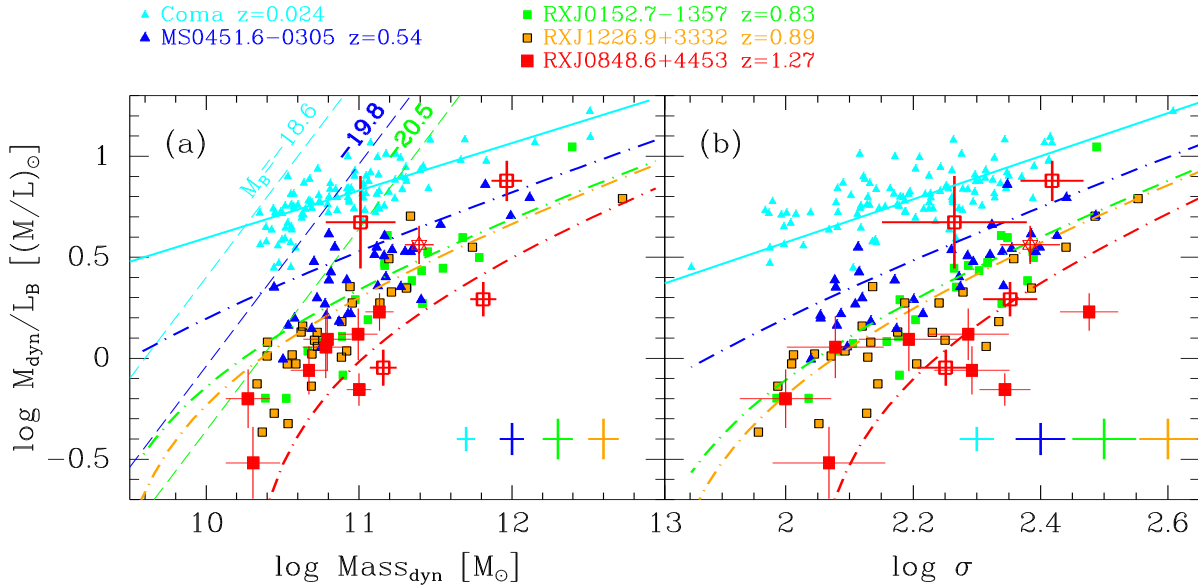


Figure 9. The dynamical M/L ratios versus the dynamical masses (a) and versus the velocity dispersions (b). Cyan line – best fit to the Coma cluster sample. Dot-dashed lines show the predicted location of the relations for each cluster redshift based on models for passive evolution with mass dependent formation redshift (Thomas et al. 2005); blue – MS0451–0305; green – RXJ0152.7–1357; orange – RXJ1226.9+3332; red – RXJ0848.6+4453. Dashed lines - selection effects. Symbols as in Fig. 7.

as reflected through the M/L versus mass relation, the absorption line strengths and the [O II] emission.

6.1. Size and velocity dispersion evolution

In our study of the massive $z = 0.5 - 0.9$ clusters also included in this paper we found no indication of evolution with redshift in sizes or velocity dispersions of the passive bulge-dominated galaxies (Jørgensen & Chiboucas 2013). Our results on RXJ0848.6+4453 presented here indicate a very small (1-sigma) difference between the sizes and velocity dispersions of galaxies at a given mass in this cluster compared to those at $z \approx 0$. A similar conclusion regarding the size evolution was reached for 16 galaxies in RXJ0848.6+4453 by Saracco et al. (2014), who using stellar masses put an upper limit on the size evolution of $r_e \propto (1+z)^{-0.1}$ equivalent to $\approx 8\%$ from $z = 1.27$ to the present.

Recent studies have addressed the question of the possible environmental dependence of the size and velocity dispersion evolution of galaxies. Several authors have directly compared sizes of passive galaxies in high density and low density environments. Lani et al. (2013) finds that at $z > 1$ galaxies in high density environments are ≈ 50 percent larger than those in low density environments. Delaye et al. (2013) reach a similar conclusion. Converting the Delaye et al. result on size dependences on redshift in the field and in clusters to a difference in sizes at $z \approx 1.3$ gives a size difference of ≈ 30 percent, with the cluster galaxies being larger. Specifically for clusters Delaye et al. find $r_e \propto (1+z)^{-0.53}$ using stellar masses, which is in agreement with the result from Saglia et al. (2010) using dynamical masses for the clusters in the EDisCS survey. At $z \approx 0$ any differences in sizes between field and cluster galaxies appear to have disappeared, or at least become undetectable, see Huertas-Company et al. (2013).

In a study of a $z \approx 1.8$ cluster, Newman et al. (2014) on the other hand find no difference between the sizes of the galaxies in that cluster and field galaxies at similar redshifts. Thus, contradicting the above results and arguing that these other

results are due to differences in the morphological mixture of the samples studied.

Of these results, only Saglia et al. (2010) use dynamical masses and their result is therefore most directly comparable to our result and also the only study that make it possible to directly compare to our results for the evolution of the velocity dispersion. On Figure 13 we summarize the results as the median offset for each of the $z = 0.5 - 1.3$ clusters relative to the location of the Coma cluster relations. The dashed lines on this figure shows the results from Saglia et al. for dynamical masses. The size and velocity dispersion evolution required to bring our RXJ0848.6+4453 to the $z \approx 0$ location of the relations with mass is only about a third of that found by Saglia et al. Formally the zero point differences relative to the Coma cluster sample are only significant at the one-sigma level.

The result from Saglia et al. is corrected for progenitor bias using a method adopted from Valentinuzzi et al. (2010). We have chosen to assess the effect of progenitor bias on our result in an empirical fashion using the information about the $H\beta$ line strength for our Coma cluster sample to evaluate the ages of galaxies in this sample. Using the model relation between the $H\beta$ line strength, age, metallicity [M/H] and abundance ratio [α /Fe] based on stellar population models from Thomas et al. (2005) and established in Jørgensen & Chiboucas (2013) we can remove galaxies from the Coma cluster sample too young to have progenitors in our RXJ0848.6+4453 sample. The difference in lookback time between the two clusters is 8.3 Gyr for our adopted cosmology. With [M/H]=0.3 and [α /Fe]=0.3 as typical average values for galaxies in the Coma cluster sample (see Jørgensen & Chiboucas 2013), we then require $\log H\beta_G \leq 0.29$ in order for the galaxies to be older than about 8.3 Gyr. Doing so reduces the zero point difference between the Coma cluster sample and our sample in RXJ0848.6+4453 for the size-mass relation to zero, while the offset for the velocity dispersion-mass relation is 0.011 in log space. These values are shown on Figure 13 as open circles. Thus, the correction for progen-

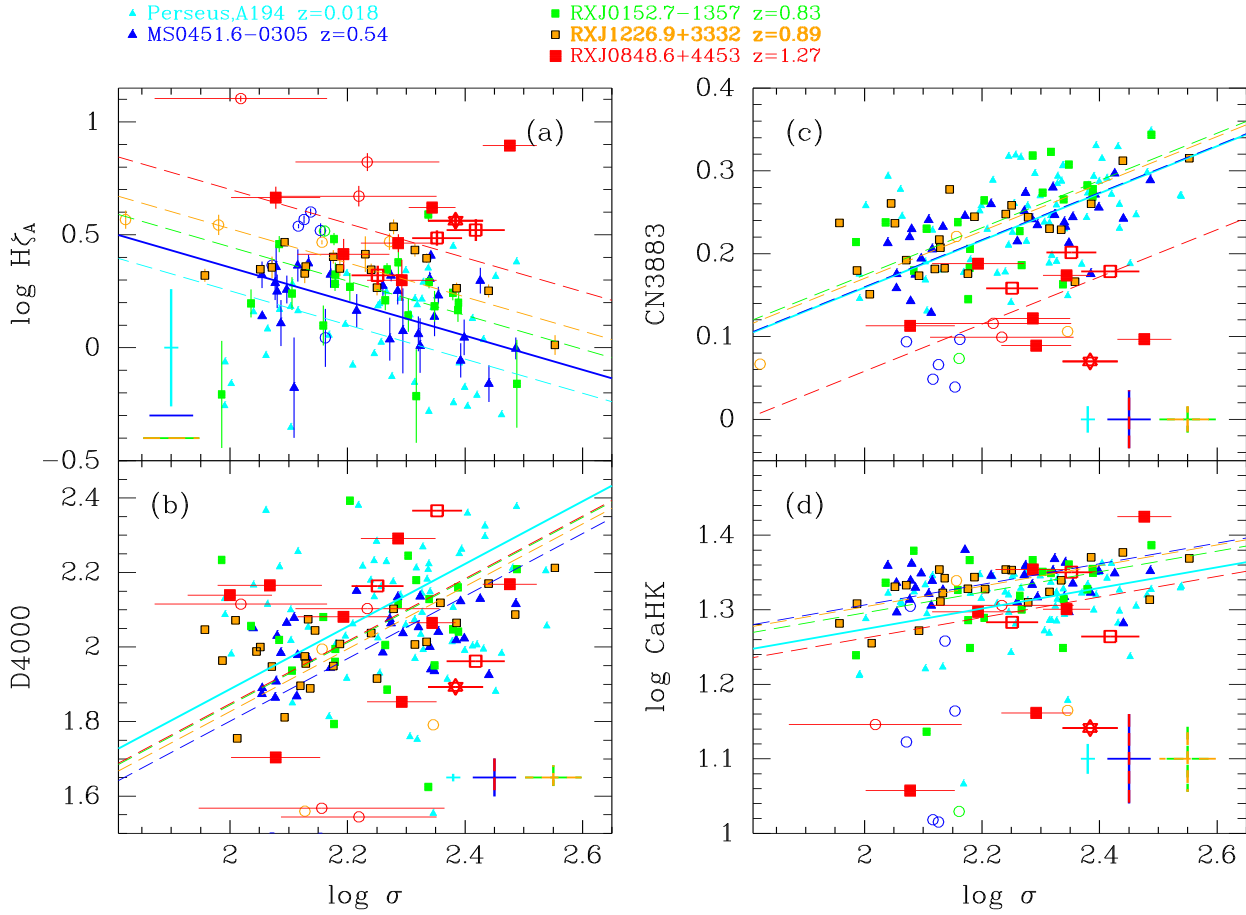


Figure 10. Absorption line strengths versus velocity dispersions. Cyan – Members of Perseus and A194; blue – MS0451.6–0305; green – RXJ0152.7–1357; orange – RXJ1226.9+3332; red – RXJ0848.6+4453. Open boxes for RXJ0848.6+4453 – galaxies with $\text{EW}[\text{O II}] > 5 \text{ \AA}$. Star – ID 2063, which hosts an AGN. In addition disk-dominated galaxies ($n_{\text{ser}} < 1.5$) are shown as open circles, color coded for cluster membership as the rest of the symbols. The solid line on each panel shows the relation for the sample used to establish the slope of the relation, while the dashed lines show the relations offset to the median zero point for each of the other clusters. The color coding of the lines match the symbols (cyan – low redshift sample; blue – MS0451–0305; green – RXJ0152.7–1357; orange – RXJ1226.9+3332; red – RXJ0848.6+4453). For D4000 all samples at $z < 1$ were used to establish the slope of the relation, see text. There are no significant zero point differences with redshift for D4000 and CaHK. For CN3883 only the offset of the RXJ0848.6+4453 sample relative to the low redshift sample is significant. All offsets for $\text{H}\zeta_{\text{A}}$ are significant, see text for discussion.

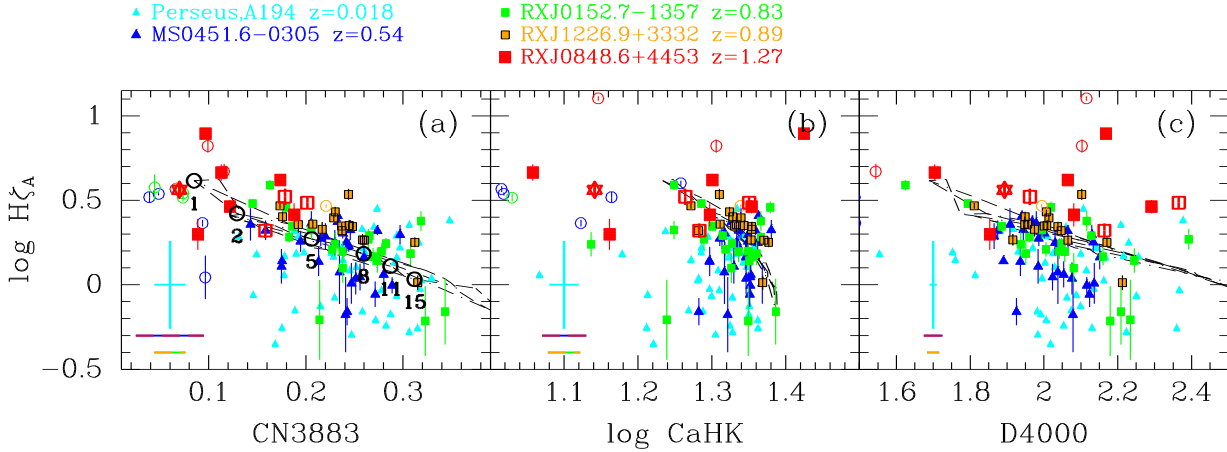


Figure 11. Absorption line strengths versus each other. Symbols as on Fig. 10. Black dashed lines – model values based on from SSPs from Maraston & Strömberg (2011). The models are degenerate in age and metallicity $[\text{M}/\text{H}]$. On panel (a) the black open circles correspond to models with solar $[\text{M}/\text{H}]$ and ages of 1, 2, 5, 8, 11, and 15 Gyr as labeled below the points, see text for details.

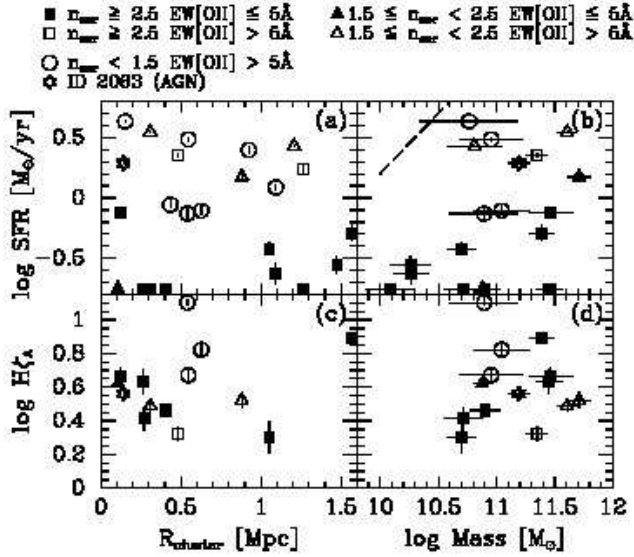


Figure 12. Star formation rates (SFR) and $\log H\zeta_A$ versus cluster center distances R_{cluster} (panels a and c) and versus the dynamical masses of the galaxies (panels b and d). The figures show data for confirmed members of RXJ0848.6+4453. Solid symbols – $\text{EW}[\text{O II}] \leq 5\text{\AA}$; open symbols – $\text{EW}[\text{O II}] > 5\text{\AA}$. Squares – $n_{\text{ser}} \geq 2.5$; triangles $1.5 \leq n_{\text{ser}} < 2.5$; circles – $n_{\text{ser}} < 1.5$; star – ID 2063, which hosts an AGN, see text. Dashed line on panel (b) – “main sequence” of star formation at $z = 0$ (Wuyts et al. 2011).

itor bias decreases the possible evolution in size and velocity dispersions, as also found by Saglia et al.

Our result for RXJ0848.6+4453 combined with our previous results for the massive $z = 0.5 - 0.9$ clusters (Jørgensen & Chiboucas 2013; also shown on Fig. 13) indicates an even larger difference between the evolution in dense environments and in the field than found by, e.g., Delaye et al. (2013). However, we note that the clusters in our $z < 1$ sample are significantly more massive than those in the EDisCS sample. Based on models for cluster mass evolution (van den Bosch 2002, see Fig. 4) RXJ0848.6+4453 is expected to evolve to a similarly massive cluster by the present time. Of the above studies, we can only confirm that Delaye et al. include some similarly massive clusters. Further, our galaxy samples in the clusters are selected consistently based on both morphology $n_{\text{ser}} > 1.5$ and spectroscopic properties (passive galaxies with $\text{EW}[\text{O II}] \leq 5\text{\AA}$). Therefore, our result cannot be explained as due to a mix-up of sample selections.

We conclude that with homogeneous selection of samples in very massive clusters, and use of dynamical galaxy masses, we find that a size and velocity dispersion evolution from $z \approx 1.3$ to the present of $\approx 16\%$ and $\approx 7\%$, respectively. Both differences are significant only at the one-sigma level. Further, the evolution is likely to have completed by $z \approx 0.9$. We put an upper limit of 23% on the increase in mass associated with this evolution (see Sect. 5.1).

6.2. Stellar population evolution

Figure 14 summarizes the changes in the M/L ratios and the absorption line strengths as the zero point offsets of the $z = 0.5 - 1.3$ cluster samples relative to the low redshift samples. All clusters are shown in these figures. Results for the $z = 0.5 - 0.9$ clusters for M/L and CN3883 are adopted from Jørgensen & Chiboucas (2013).

We compare the zero point for the M/L-Mass relation

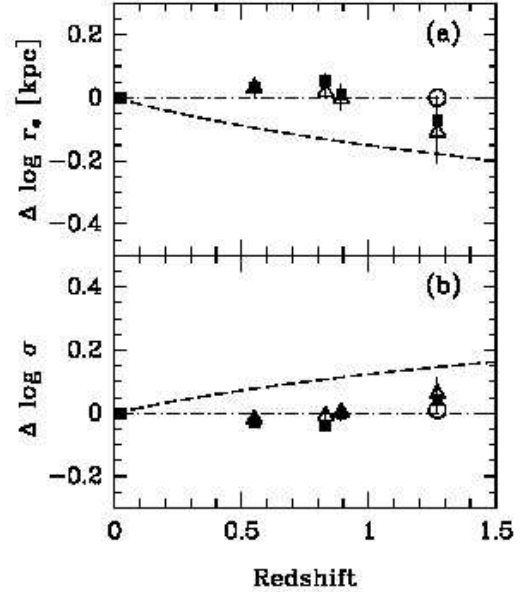


Figure 13. Zero point offsets for size-Mass and velocity dispersion-Mass relations as a function of cluster redshifts. Solid boxes – based on effective radii from $r^{1/4}$ profile fits; triangles – based on effective radii from fits with Sérsic profiles; open circles for RXJ0848.6+4453 only – offset relative to the Coma cluster sample when galaxies younger than $\approx 8.3\text{Gyr}$ are removed from the Coma cluster sample. Dashed lines – results from Saglia et al. (2010); dot-dashed lines – reference for no evolution. Without correcting for progenitor bias due to the presence of young galaxies in the Coma cluster sample, RXJ0848.6+4453 at $z = 1.27$ shows roughly a third the evolution with redshift compared to the results from Saglia et al. With correction for progenitor bias, there is no evolution with redshift, see text for discussion.

for the RXJ0848.6+4453 bulge-dominated galaxies with $\text{EW}[\text{O II}] \leq 5\text{\AA}$ to that of the Coma cluster sample. The difference is consistent with passive evolution and a formation redshift of $z_{\text{form}} = 1.95^{+0.22}_{-0.15}$. This is higher than for the $z = 0.5 - 0.9$ clusters (Jørgensen & Chiboucas 2013, see also Fig. 14a) for which we found $z_{\text{form}} \approx 1.4$. The difference becomes even larger, when considering that the eight passive galaxies in our RXJ0848.6+4453 all have masses below $10^{11.1} M_{\odot}$. For similar low-mass galaxies in the $z = 0.5 - 0.9$ clusters the formation redshift is ≈ 1.2 (blue points on Fig. 14a).

We speculate that the reason for this difference is that a large fraction of the low mass galaxies in $z = 0.5 - 0.9$ clusters have entered the passive bulge-dominated population more recently than $z \approx 1.3$. Thus, the difference is due to a progenitor bias. The RXJ0848.6+4453 sample does not include the progenitors of those young bulge-dominated galaxies in the $z = 0.5 - 0.9$ clusters, as such progenitors observed at $z \approx 1.3$ would have very strong star formation and maybe also not yet be bulge-dominated. This conclusion is similar to that reached by Sánchez-Blázquez et al. (2009) who argue that 50% of the low mass galaxies on the red sequence at low redshift have entered the red sequence recently.

Turning to the strength of the $H\zeta$ line, our results support the idea that RXJ0848.6+4453 experienced a major episode of star formation 1-2 Gyr prior, consistent with $z_{\text{form}} = 1.95$. The strengths of $H\zeta$ seen in the RXJ0848.6+4453 galaxies can according to stellar population models only be achieved for such young stellar populations (see Fig. 11a). Within the uncertainty, this is also consistent with the zero point offset

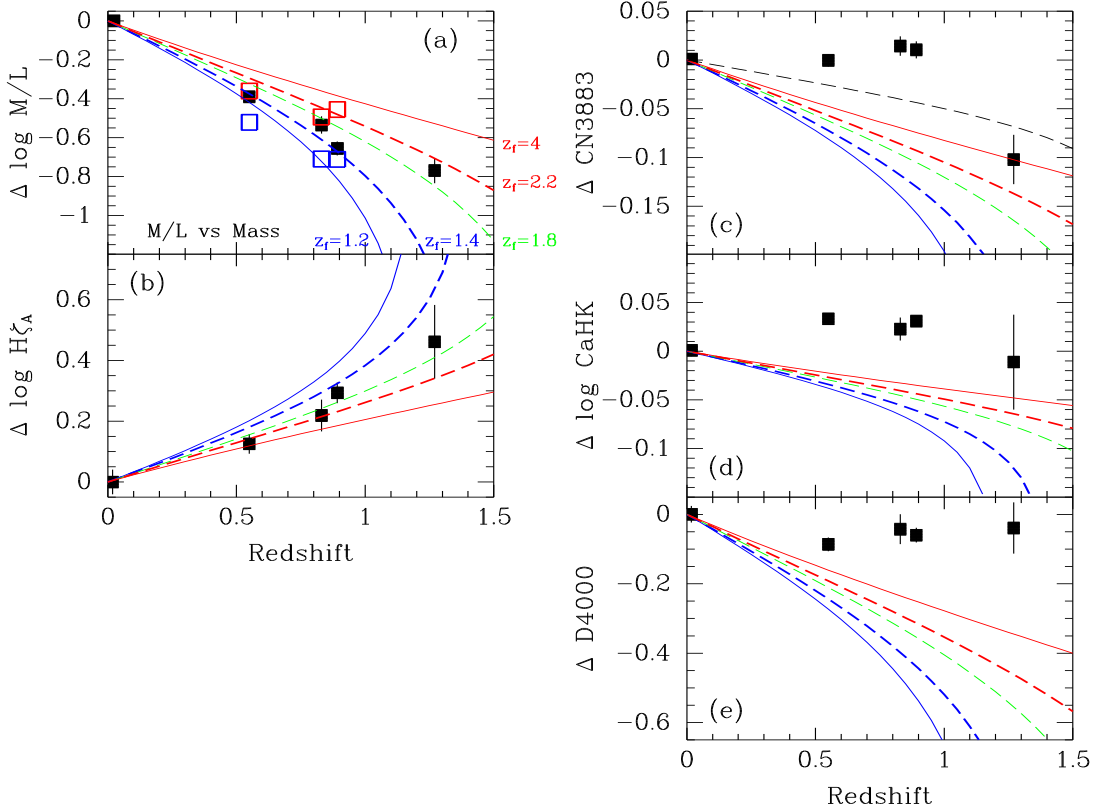


Figure 14. The zero point offsets of the scaling relations for the $z = 0.5 - 1.3$ cluster samples relative to the low redshift samples, shown as a function of redshift. Results for the $z < 1$ clusters for the M/L ratios and CN3883 are adopted from Jørgensen & Chiboucas (2013). Predictions from models for passive evolution based on models from Maraston (2005) and Maraston & Strömbäck (2011) are overlaid, labeled with the assumed formation redshift z_{form} . Black dashed line on panel (c) – the prediction for $z_{\text{form}} = 1.8$ if adopting the age dependence of CN3883 discussed in Jørgensen & Chiboucas (2013). Black points – median for the full sample in each cluster; red points – for $z = 0.5 - 0.9$ clusters, galaxies with $\log \text{Mass} \geq 11$; blue points – for $z = 0.5 - 0.9$ clusters, galaxies with $\log \text{Mass} < 11$.

of the $H\zeta_A$ –velocity dispersion relation for RXJ0848.6+4453 relative to the low redshift sample (Fig. 14b). The occurrence of such a star formation episode is further supported by the fact that the most massive bulge-dominated galaxies in the cluster all have significant [O II] emission.

It is worth noting that all the bulge-dominated galaxies show young stellar populations either through the strength of the $H\zeta$ line or presence of [O II] emission, or both. These galaxies are distributed throughout the cluster (see Fig. 12). Thus, there is no indication that the star formation has yet been quenched in the center of the cluster. This is different from results for the more massive clusters RDCS J1252.9–2927 ($z = 1.24$) and XMMU J2235.3–2557 ($z = 1.4$) at similar redshifts. Both of these clusters show an absence of star forming galaxies in the very center of the clusters (Nantais et al. 2013; Grützbauch et al. 2012). We speculate that the difference is related to the mass of the clusters, as these two latter clusters have $M_{500} = 6.1 \times 10^{14} M_{\odot}$ (Stott et al. 2010) and $M_{500} = 4.4 \times 10^{14} M_{\odot}$ (Rosati et al. 2009, see also Stott et al. 2010), respectively. Thus, masses that are a factor 3–4.5 larger than the mass of RXJ0848.6+4453. Lynx E, which is located in the same supercluster as RXJ0848.6/4453/Lynx W, and is similarly massive as RDCS J1252.9–2927 and XMMU J2235.3–2557 ($M_{500} = 4.7 \times 10^{14} M_{\odot}$, Stott et al. 2010) has not yet been studied in the same detail.

Two studies of $z \approx 2$ clusters find similar results regarding

the presence of star formation in massive cluster galaxies as we find for RXJ0848.6+4453. Strazzullo et al. (2013) find in their study of J1449+0856 ($z = 2.0$) that the cluster hosts massive star forming as well as passive galaxies in the core. This cluster has an estimated mass of $M_{500} = 3.4 \times 10^{13} M_{\odot}$ (Gobat et al. 2011, with the conversion $M_{200} \approx 1.54 M_{500}$ from Brodwin et al. 2011). Thus, the cluster is significantly less massive than RXJ0848.6+4453, but based on the models for cluster mass evolution with redshift (see Fig. 4) it is expected to evolve into a cluster mass similar to that of RXJ0848.6+4453 at $z \approx 1.3$.

Tanaka et al. (2013) investigated the cluster galaxies around the radio source PKS1138–262 ($z = 2.16$) and conclude that this cluster also contains a mix of massive star forming and passive galaxies, as if the cluster is in the process of quenching the star formation. Shimakawa et al. (2014) derived the velocity dispersion of $H\alpha$ and $Ly\alpha$ emitters that they consider part of the virialized core of the cluster. They find $\sigma_{\text{cluster}} = 683 \text{ km s}^{-1}$ from which they derive $M_{200} = 1.71 \times 10^{14} M_{\odot}$, or $M_{500} = 1.1 \times 10^{14} M_{\odot}$ with the conversion from Brodwin et al. This cluster mass represents an upper limit as even the core may not yet be virialized. However, it appears that the cluster may already have a mass comparable to that of RXJ0848.6+4453 and therefore will be expected to evolve into a significantly more massive cluster than RXJ0848.6+4453 at later epochs.

The difference in lookback time between $z \approx 2$ and $z \approx 1.3$ is about 1.5 Gyr with our adopted cosmology. Thus, it is plausible that we are in fact seeing J1449+0856, PKS1138–262 and RXJ0848.6+4453 at slightly different epochs during the quenching of the star formation as the galaxies fall into the dense cluster environment. We speculate that this process takes place earlier (or faster) in more massive clusters like RDCS J1252.9–2927 and XMMU J2235.3–2557. Detailed spectroscopic observations of both those two clusters and higher redshift progenitors, of such massive clusters are needed to resolve this question. Based on its mass estimate PKS1138–262 may be such a progenitor.

The results for the M/L ratios, H ζ line strength and [O II] emission appear to give a consistent picture of the stellar populations in the bulge-dominated RXJ0848.6+4453 galaxies and an epoch of the period of the last star formation of $z_{\text{form}} = 1.95$. However, the strengths of the metal lines CN3883 and CaHK, as well as the D4000 strength appear in contradiction with these results. These three indices are all stronger than expected for 1-2 Gyr old stellar populations with metallicities of $[M/H] = 0-0.3$, based on the predictions from SEDs from Maraston & Strömbäck (2011). This is shown in Figure 14c-e, where we show the zero point offsets for these three indices relative to our low redshift sample. The figure also shows the results for the $z = 0.5-0.9$ clusters from Jørgensen & Chiboucas (2013). As our RXJ0848.6+4453 sample is the first sample of $z > 1$ galaxies with measured metal absorption line indices, we cannot compare this result to any prior results. We do caution that the stellar population models may not correctly model these blue indices. In Jørgensen & Chiboucas (2013) we showed that the SEDs from Maraston & Strömbäck predict CN3883 too strong for a given CN₂ index. Because of that, the prediction of the age dependency for CN3883 based on these SEDs is also significantly stronger than if we adopt the dependency derived from the CN₂ index as we did in Jørgensen & Chiboucas (2013). On Figure 14c we show this latter prediction as well for $z_{\text{form}} = 1.8$. From this it is clear that it is yet not straight forward to interpret the strength of this blue metal index within the frame work of the SSP models. Thus, to make progress on the interpretation of the metal indices, further progress is needed on the modeling. This is beyond the scope of this paper. Additional data for $z > 1$ cluster galaxies are also needed to confirm the presence of these strong metal lines in galaxies at these redshifts.

7. CONCLUSIONS

We have used deep ground-based optical spectroscopy from Gemini North and *HST*/ACS imaging to investigate the structure and stellar populations of galaxies in RXJ0848.6+4453/Lynx W at redshift $z = 1.27$. Our main conclusions are as follows:

1. At a given dynamical mass, the galaxies in RXJ0848.6+4453 show only a very small difference in size and velocity dispersion when compared to our low redshift sample. Formally the effects are at the one-sigma level and about one third of that expected if extrapolating the results from the EDisCS survey (Saglia et al. 2010). Our result adds support to the idea that the evolution of sizes and velocity dispersions depends on the cluster environment and is accelerated in high mass clusters compared to poorer clusters and the field.
2. The bulge-dominated galaxies in RXJ0848.6+4453

populate a Fundamental Plane (FP) similar to that seen for lower redshift galaxies. The slope for the RXJ0848.6+4453 is similar to that found for $z = 0.8-0.9$ clusters, though the sample is too small for an independent determination of the slope. The FP zero point is in agreement with a model of passive evolution with a formation redshift of $z_{\text{form}} = 1.95^{+0.22}_{-0.15}$. This is a higher z_{form} than we previously found for our sample of galaxies in $z = 0.8-0.9$ clusters at similar galaxy masses (Jørgensen & Chiboucas 2013). Our result show that the low mass end of the FP is populated already at $z \approx 1.3$, but also that additional passive galaxies are added at later epochs.

3. The bulge-dominated galaxies in RXJ0848.6+4453 have very strong H ζ absorption lines and the highest mass bulge-dominated galaxies also contain significant [O II] emission. From both of these facts, we conclude that the galaxies have experienced an episode of star formation about 1-2 Gyr prior to the epoch equivalent to the cluster redshift. This is in agreement with the formation redshift determined from the FP. The data indicate that this episode of star formation was widespread in the cluster, and that star formation has not yet been fully quenched in the very center of the cluster.
4. The metal lines CN3883 and CaHK, as well as D4000 are stronger than expected if these galaxies have $z_{\text{form}} = 1.95$ and are to passively evolve into galaxies similar to those in our lower redshift samples. Further investigation of metal lines in $z > 1$ galaxies are needed to shed light on this apparent contradiction with the results from the FP zero point and H ζ strengths.

Our comparison of the stellar populations in the RXJ0848.6+4453 galaxies with that of more massive clusters at similar redshift and with less massive clusters at higher redshift raise the possibility that the quenching of star formation in the cluster galaxies depend on the cluster properties. The quenching may either happen earlier or faster in the more massive clusters. Detailed spectroscopic investigations of additional massive clusters at $z = 1-2$ are required to shed further light on this issue.

Acknowledgments: Karl Gebhardt is thanked for making his kinematics software available. Masayuki Tanaka is thanked for alerting us to the most recent mass estimate for PKS1138–262. We thank the anonymous referee for constructive suggestions that helped improve this paper. The Gemini TACs and the former Director Fred Chaffee are thanked for generous time allocations to carry out these observations.

Based on observations obtained at the Gemini Observatory, which is operated by the Association of Universities for Research in Astronomy, Inc., under a cooperative agreement with the NSF on behalf of the Gemini partnership: the National Science Foundation (United States), the National Research Council (Canada), CONICYT (Chile), the Australian Research Council (Australia), Ministério da Ciência e Tecnologia (Brazil) and Ministerio de Ciencia, Tecnología e Innovación Productiva (Argentina)

The data presented in this paper originate from the following Gemini programs: GN-2011B-DD-3, GN-2011B-DD-5, and GN-2013A-Q-65. In part, based on observations made

with the NASA/ESA Hubble Space Telescope, obtained from the data archive at the Space Telescope Science Institute.

I.J. acknowledge support from grant HST-AR-13255.01 from STScI. STScI is operated by the Association of Universities for Research in Astronomy, Inc. under NASA contract NAS 5-26555.

REFERENCES

- Abraham, R., Glazebrook, K., McCarthy, P. J., et al. 2004, *AJ*, 127, 2455
- Beers, T. C., Flynn, K., & Gebhardt, K. 1990, *AJ*, 100, 32
- Bender, R., Burstein, D., & Faber, S. M. 1992, *ApJ*, 399, 462
- Bertin, E., & Arnouts, S. 1996, *A&AS*, 117, 393
- Blanton, M. R., Brinkmann, J., Csabai, I., et al. 2003, *AJ*, 125, 2348
- Brodwin, M., Stern, D., Vikhlinin, A., et al. 2011, *ApJ*, 732, 33
- Bruzual, G., & Charlot, S. 2003, *MNRAS*, 344, 1000
- Cappellari, M., Bacon, R., Bureau, M., et al. 2006, *MNRAS*, 366, 1126
- Cassata, P., Giavalisco, M., Williams, C. C., et al. 2013, *ApJ*, 775, 106
- Chiboucas, K., Barr, J., Flint, K., Jørgensen, I., Collobert, M., & Davies, R. 2009, *ApJS*, 184, 271
- Ciotti, L., 1991, *A&A*, 249, 99
- Davidge, T. J., & Clark, C. C. 1994, *AJ*, 107, 946
- Delaye, L., Huertas-Company, H., Mei, S., et al. 2013, arXiv:1307.0003
- Djorgovski, S., & Davis, M. 1987, *ApJ*, 313, 59
- Ettori, S., Tozzi, P., Borgani, S., & Rostati, P. 2004, *A&A*, 417, 13
- Fakhouri, O., Ma, C.-P., Boylan-Kolchin, M. 2010, *MNRAS*, 406, 2267
- Fruchter, A. S., & Hook, R. N. 2002, *PASP*, 114, 144
- Gallagher, J. S., Bushouse, H., Hunter, D. A. 1989, *AJ*, 97, 700
- Gebhardt, K., Richstone, D., Kormendy, J., et al. 2000, *AJ*, 119, 1157
- Gebhardt, K., Faber, S. M.; Koo, D. C., et al. 2003, *ApJ*, 597, 239
- Gobat, R., Daddi, E., Onodera, M. et al. 2011, *A&A*, 526, A133
- Gobat, R., Strazzullo, V., Daddi, E., et al. 2013, *ApJ*, 776, 9
- Gorgas J., Cardiel N., Pedraz S., & González J. J. 1999, *A&AS*, 139, 29
- Grützbauch, R., Bauer, A. E., Jørgensen, I., Varela, J. 2011, *MNRAS*, 423, 3652
- Hook, I. M., Jørgensen, I., Allington-Smith, J. R., et al. 2004, *PASP*, 116, 425
- Huertas-Company, M., Shankar, F., Mei, S., et al. 2013, *ApJ*, 779, 29
- Jørgensen, I. 1999, *MNRAS*, 306, 607
- Jørgensen, I., & Chiboucas, K. 2013, *AJ*, 145, 77
- Jørgensen, I., Franx, M., & Kjaergaard, P. 1995a, *MNRAS*, 273, 1097
- Jørgensen, I., Franx, M., & Kjaergaard, P. 1995b, *MNRAS*, 276, 1341
- Jørgensen, I., Franx, M., & Kjaergaard, P. 1996, *MNRAS*, 280, 167
- Jørgensen, I., Bergmann, M., Davies, R., Barr, J., Takamiya, M., & Crampton, D. 2005, *AJ*, 129, 1249
- Jørgensen, I., Chiboucas, K., Flint, K., Bergmann, M., Barr, J., & Davies, R. 2006, *ApJL*, 639, L9
- Jørgensen, I., Chiboucas, K., Flint, K., Bergmann, M., Barr, J., & Davies, R. 2007, *ApJL*, 654, L179
- Kennicutt Jr., R. C. 1992, *ApJ*, 388, 310
- Koyama, Y., Smail, I., Kurk, J. et al. 2013, *MNRAS*, 434, 423
- Krist, J. 1995, in ASP Conf. Ser. 77, *Astronomical Data Analysis Software and Systems IV*, ed. R. A. Shaw, H. E. Payne, & J. J. E. Hayes (San Francisco, CA: ASP), 349
- Kuntschner, H. 2000, *MNRAS*, 315, 184
- Kurk, J., Cimatti, A., Zamorani, G. et al. 2009, *A&A*, 504, 331
- Lani, C., Almaini, O., Hartley, W. G., et al. 2013, *MNRAS*, 435, 207
- Lord, S. D., 1992, *NASA Technical Memorandum*, 103957
- Maraston, C. 2005, *MNRAS*, 362, 799
- Maraston, C., Strömbäck, G. 2011, *MNRAS*, 418, 2785
- Mignoli, M., Vignali, C., Gilli, R., et al. 2013, *A&A*, 556, A29
- Monet, D., et al. 1998, *VizieR Online Data Catalog*, 1252, <http://vizier.cfa.harvard.edu/viz-bin/VizieR?-source=I/252>
- Nantais, J. B., Rettura, A., Lidman, C., et al. 2013, *A&A*, 556, 112
- Newman, A. B., Ellis, R. S., Bundy, K., & Treu, T. 2012, *ApJ*, 746, 162
- Newman, A. B., Ellis, R. S., Andreon, S., et al. 2014, *ApJ*, 788, 51
- Papovich, C., Bassett, R., Lotz, J. M., et al. 2012, *ApJ*, 750, 93
- Peng, C. Y., Ho, L. C., Impey, C. D., & Rix, H.-W. 2002, *AJ*, 124, 266
- Piffaretti, R., Arnaud, M., Pratt, G. W., Pointecouteau, & Melin, J.-B. 2011, *A&A*, 534, A109
- Quadri, R. F., Williams, R. J., Franx, M., Hildebrandt, H. 2012, *ApJ*, 744, 88
- Rosati, P., Tozzi, P., Gobat, R., et al. 2009, *A&A*, 508, 583
- Saglia, R. P., Maraston, C., Greggio, L., Bender, R., Ziegler, B. 2000, *A&A*, 360, 911
- Saglia, R. P., Sánchez-Blázquez, P., Bender, R., et al. 2010, *A&A*, 524, A6
- Salpeter, E. E. 1955, *ApJ*, 121, 161
- Sánchez-Blázquez, P., Jablonka, P., Noll, S., et al. 2009, *A&A*, 499, 47
- Saracco, P., Casati, A., Gargiulo, G., et al. 2014, arXiv:1401.5600
- Schlafly, E. J., et al. 2011, *ApJ*, 737, 103
- Sérsic, J. L. 1968, *Atlas de Galaxias Australes* (Cordoba: Observatorio Astronomico)
- Shimakawa, R., Kodama, T., Tadaki, K., et al. 2014, *MNRAS*, tmpL, 56
- Sirianni, M., Jee, M. J., Benítez, N., et al. 2005, *PASP*, 117, 1049
- Schmidt, M., Hasinger, G., Gunn, J., et al. 1998, *A&A*, 329, 495
- Sparks, W. B., Jørgensen, I. 1993, *AJ*, 105, 1735
- Stanford, S. A., Brodwin, M., Gonzalez, A. H., et al. 2012, *ApJ*, 753, 164
- Stott, J., Collins, C., Sahlén, M., et al. 2010, *ApJ*, 718, 1
- Strazzullo, V., Gobat, R., Daddi, E., et al. 2013, *ApJ*, 772, 118
- Tanaka, M., Toft, S., Marchesini, D., et al. 2013, *ApJ*, 772, 113
- Thomas, D., Maraston, C., Bender, R., & de Oliveira, C. M. 2005, *ApJ*, 621, 673
- Toft, S., Franx, M., van Dokkum, P., et al. 2009, *ApJ*, 705, 255
- Toft, S., Gallazzi, A., Zirm, A., Wold, M., Zibetti, S., Grillo, C., Man, A. 2012, *ApJ*, 754, 3
- Valentinuzzi, T., Fritz, J., Poggianti, B. M., et al. 2010, *ApJ*, 712, 226
- van den Bosch, F. C. 2002, *MNRAS*, 331, 98
- van der Wel, A., Franx, M., van Dokkum, P. G., et al. 2014, arXiv:1404.2844
- van Dokkum, P. G., & Franx, M. 2001, *ApJ*, 553, 90
- van Dokkum, P. G., Whitaker, K. E., Brammer, G., et al. 2010, *ApJ*, 709, 1018
- Vikhlinin, A., Burenin, R. A., Ebeling, H., et al. 2009, *ApJ*, 692, 1033
- Wuyts, S., Förster Schreiber, N., van der Wel, A., et al. 2011, *ApJ*, 742, 96
- Zabludoff, A., Huchra, J. P., & Geller, M. J. 1990, *ApJS*, 74, 1
- Zirm, A. W., Toft, S., Tanaka, M. 2012, *ApJ*, 744, 181

APPENDIX

PHOTOMETRY FROM *HST*/ACS

Table 10 lists the photometric parameters for the spectroscopic sample as derived from the *HST*/ACS observations in F850LP and F775W. Only the F850LP images were processed to derive 2-dimensional surface photometry using GALFIT (Peng et al. 2002). F775W was used only for the color determinations. The effective radii in Table 10 are derived from the semi-major and -minor axes as $r_e = (a_e b_e)^{1/2}$. The difference between the effective radii from fits with an $r^{1/4}$ -profile and a Sérsic profile should not be interpreted as the uncertainty. As expected the difference is correlated with the Sérsic index, n_{ser} , see Figure 15.

Figure 16 shows our photometric parameters compared with those from Saracco et al. (2014) for the eight galaxies in common. We have offset the $z_{850, \text{Vega}}$ magnitudes from Saracco et al. (2014) to AB magnitudes using the synthetic zero points from Sirianni et al. (2005). As the errors on total magnitudes and effective radii are strongly correlated, we show the differences in the logarithm of the effective radii (in kpc) versus the difference in the total z_{850} magnitudes. The solid line shows the best fit relation. From zero point of this fit we can derive the magnitude difference between our magnitudes and those of Saracco et al. (2014) as 0.04 ± 0.03 mag. This very small difference is most likely due to the difference in the choice of point-spread-function (PSF). Saracco et al. uses a PSF constructed from stars in the field, while we use Tiny Tim (Krist 1995) model PSFs (see Chiboucas et al. 2009).

We have derived total magnitudes in the rest frame B-band from the observed z_{850} magnitudes and colors, using calibrations established based on Bruzual & Charlot (2003) stellar population models spanning the observed color range, see Jørgensen et al. (2005) for details. We use the aperture color ($i_{775} - z_{850}$) in the calibration, and calibrate all total magnitudes to the rest

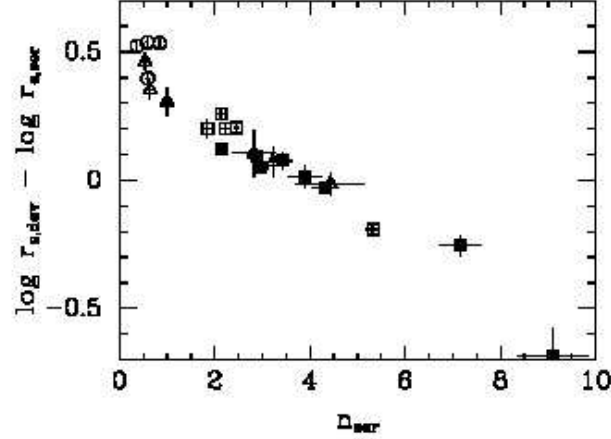


Figure 15. The difference $\log r_{e,\text{dev}} - \log r_{e,\text{ser}}$ versus the Sérsic index, n_{ser} . Solid squares – bulge-dominated galaxies with $\text{EW}[\text{O II}] \leq 5\text{\AA}$; open squares – bulge-dominated galaxies with $\text{EW}[\text{O II}] > 5\text{\AA}$; circles - disk-dominated galaxies; triangles - galaxies with $S/N < 10$ in the spectroscopic observations and therefore excluded from the analysis. As expected the figure shows a correlation, with the effective radius from the Sérsic fits being larger than those from the fits with $r^{1/4}$ -profiles if $n_{\text{ser}} > 4$.

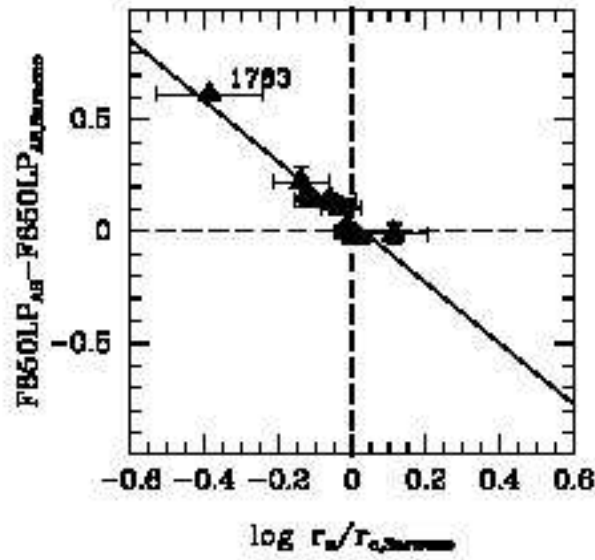


Figure 16. Comparison of our *HST* photometry with that of Saracco et al. (2014) for the eight galaxies in common, show as the difference in the logarithm of the effective radii versus the difference in total magnitudes. The errors in the two parameters are strongly correlated. Solid line – best fit relation. The zero point difference between our magnitudes and those of Saracco et al. (2014) as 0.04 ± 0.03 mag.

frame B-band using this color. This ignores any effects of color gradients, but is preferable because the aperture color has lower uncertainty than the total color. For the cluster redshift the calibration is

$$B_{\text{rest}} = z_{850} + 1.390 - 1.144(i_{775} - z_{850}) \quad (\text{A1})$$

The large color term is due to the fact that at the cluster redshift the F850LP filter spans the 4000\AA break. The distance modulus for our adopted cosmology is $DM(z) = 44.74$. The absolute B-band magnitude, M_B , is then derived as

$$M_B = B_{\text{rest}} - DM(z). \quad (\text{A2})$$

Techniques for how to calibrate to a “fixed-frame” photometric system are described in detail by Blanton et al. (2003).

Table 10
RXJ0848.6+4453: Photometric Parameters from *HST*/ACS data

ID (1)	RA (J2000) (2)	DEC (J2000) ^a (3)	$m_{\text{tot,SEx}}$ (4)	$(i_{775} - z_{850})$ (5)	$m_{\text{tot,dev}}$ (6)	$\log r_{e,\text{dev}}$ (7)	$m_{\text{tot,ser}}$ (8)	$\log r_{e,\text{ser}}$ (9)	n_{ser} (10)	PA (11)	ϵ (12)
240	8 48 48.20	44 52 08.9	23.00	1.068	22.85	-0.807	22.56	-0.553	7.2	28.3	0.19
336	8 48 47.33	44 51 47.5	24.53	0.950	24.52	-0.596	24.41	-0.713	1.7	-29.4	0.70
361	8 48 49.26	44 54 17.3	22.29	0.903	21.97	-0.215	21.94	-0.189	4.2	72.9	0.13
438	8 48 46.12	44 51 23.8	24.46	0.527	23.74	-0.076	24.35	-0.499	1.4	81.7	0.11
634	8 48 46.59	44 53 17.0	24.14	0.556	24.03	-0.582	24.31	-0.776	0.9	43.3	0.64
654	8 48 46.74	44 53 36.6	24.71	0.535	24.35	-0.424	24.48	-0.528	2.8	-0.5	0.73
661	8 48 47.17	44 54 28.7	21.20	0.748	20.76	-0.114	21.05	-0.330	2.2	-16.6	0.36
722	8 48 44.91	44 52 26.6	23.49	0.710	22.66	0.097	23.50	-0.466	0.6	-46.5	0.65
807	8 48 44.27	44 52 22.8	24.18	0.625	23.79	-0.506	24.05	-0.708	1.9	12.4	0.42
887	8 48 45.59	44 54 30.7	24.25	0.018	23.60	-0.193	23.96	-0.453	2.1	-28.6	0.60
1044	8 48 43.29	44 53 48.4	22.84	0.550	22.20	-0.157	22.85	-0.602	0.6	51.5	0.67
1045	8 48 42.94	44 53 06.6	24.37	0.042	23.78	-0.363	24.32	-0.729	0.7	-60.1	0.51
1123	8 48 41.81	44 52 45.4	24.10	0.658	23.43	-0.150	24.11	-0.613	0.5	9.0	0.29
1173	8 48 42.73	44 54 17.3	23.49	0.549	22.81	-0.181	23.44	-0.615	0.4	-59.1	0.39
1177	8 48 40.36	44 51 56.3	23.78	0.552	23.14	-0.143	23.74	-0.575	0.6	-54.2	0.38
1264	8 48 39.66	44 51 49.0	23.92	0.827	23.68	-0.712	23.70	-0.724	3.9	-85.3	0.05
1276	8 48 40.07	44 52 50.4	22.76	0.296	22.18	-0.019	22.71	-0.406	0.7	71.2	0.84
1352	8 48 39.28	44 52 10.8	24.78	0.569	24.32	-0.266	24.67	-0.535	1.4	-59.8	0.81
1362	8 48 38.64	44 52 12.5	24.38	0.728	22.03	0.143	22.34	-0.114	2.1	50.0	0.58
1517	8 48 39.36	44 53 44.8	23.05	0.804	22.87	-0.412	22.86	-0.413	3.8	18.7	0.49
1533	8 48 40.81	44 55 11.4	24.59	0.682	24.01	-0.401	24.55	-0.753	0.6	22.1	0.63
1644	8 48 37.96	44 54 02.4	23.19	0.916	21.72	0.392	22.31	-0.132	0.4	71.3	0.35
1698	8 48 37.45	44 53 26.7	24.45	0.557	24.07	-0.689	24.37	-0.893	1.5	10.4	0.57
1748	8 48 37.07	44 53 33.9	23.09	0.950	22.81	-0.566	22.93	-0.658	2.9	24.1	0.39
1763	8 48 35.97	44 53 36.0	21.70	1.043	21.32	0.120	21.56	-0.085	2.4	-83.6	0.24
1809	8 48 36.96	44 53 56.2	24.45	0.975	23.99	-0.256	24.36	-0.562	1.0	-72.4	0.50
1888	8 48 36.16	44 54 17.2	22.12	0.949	22.00	-0.331	21.76	-0.139	5.3	-25.4	0.24
2015	8 48 34.05	44 53 02.4	24.43	0.909	24.24	-1.125	24.21	-1.110	4.4	57.2	0.13
2063	8 48 34.07	44 53 32.2	23.17	0.803	22.75	-0.361	23.01	-0.563	2.2	40.2	0.28
2111	8 48 33.57	44 53 44.0	23.10	0.666	22.87	-0.359	22.10	0.324	9.1	-71.6	0.34
2138	8 48 33.31	44 53 27.0	24.06	0.529	23.54	-0.256	24.14	-0.662	0.8	86.7	0.52
2336	8 48 26.67	44 53 19.0	21.71	0.647	21.21	-0.005	21.61	-0.304	1.6	16.5	0.59
2342	8 48 27.94	44 54 51.0	24.89	0.542	24.86	-0.644	24.88	-0.832	0.6	47.3	0.83
2369	8 48 29.39	44 54 41.8	24.30	1.015	22.94	-0.014	23.50	-0.412	0.6	-36.4	0.82
2417	8 48 28.24	44 54 22.1	23.31	0.790	22.53	0.063	23.35	-0.471	0.8	-41.0	0.51
2450	8 48 28.59	44 54 41.5	24.03	0.970	23.83	-1.046	23.83	-1.046	4.0	-61.3	0.31
2497	8 48 26.93	44 54 30.2	24.17	0.607	23.87	-0.641	2.8	-86.2	0.35
2600	8 48 33.00	44 55 11.8	23.14	0.945	22.92	-0.600	22.67	-0.386	6.2	16.3	0.32
2624	8 48 28.69	44 53 03.0	24.31	0.828	24.11	-0.736	24.06	-0.698	4.5	10.0	0.22
2651	8 48 30.56	44 54 54.9	23.44	0.778	22.12	-0.013	22.97	-0.582	0.3	-4.2	0.35
2702	8 48 29.68	44 53 23.9	24.33	0.959	24.03	-0.627	24.12	-0.698	3.2	-18.3	0.16
2735	8 48 27.43	44 55 28.4	23.32	0.944	23.16	-0.899	23.12	-0.871	4.3	-62.1	0.49
2772	8 48 30.79	44 53 34.8	23.03	0.568	22.27	0.003	23.07	-0.535	0.6	-76.9	0.54
2943	8 48 32.76	44 54 07.1	23.42	0.862	23.15	-0.581	23.25	-0.659	3.4	78.5	0.36
2989	8 48 24.42	44 56 09.0	23.16	0.932	22.90	-0.816	22.98	-0.863	3.0	27.5	0.59
3030	8 48 32.74	44 54 45.4	22.71	1.075	22.12	0.093	22.50	-0.209	1.8	47.5	0.33
3074	8 48 21.17	44 54 33.1	22.81	1.003	22.66	-0.723	22.53	-0.610	5.5	-21.0	0.52
3090	8 48 32.97	44 53 46.6	22.49	0.971	22.16	-0.675	22.34	-0.798	2.2	80.0	0.51
3144	8 48 21.37	44 54 32.6	24.12	0.501	22.73	-0.307	23.18	-0.615	0.8	-78.3	0.64
3384	8 48 26.54	44 55 18.5	23.12	0.733	22.14	0.299	22.56	0.004	2.5	-49.6	0.20
3426	8 48 25.51	44 55 46.4	23.88	0.829	23.58	-0.614	> 4 ^a	72.3	0.47
3461	8 48 24.70	44 54 13.8	22.91	0.975	22.40	-0.110	22.95	-0.468	0.9	13.0	0.12
3505	8 48 22.87	44 53 20.5	23.41	0.851	22.32	-0.293	22.95	-0.696	1.0	17.0	0.24
9001	8 48 19.43	44 53 46.5	24.32	0.508	24.36	-0.523	24.66	-0.709	1.4	-44.6	0.77

Note. — Col. (1) Galaxy ID; col. (2) and (3) Positions consistent with USNO (Monet et al. 1998), with an rms scatter of ≈ 0.5 arcsec. col. (4) total F850LP magnitude from SExtractor; col. (5) Aperture color within an aperture with radius 0.5 arcsec; col. (6) total magnitude from fit with $r^{1/4}$ profile; col. (7) logarithm of the effective radius in arcsec from fit with $r^{1/4}$ profile; col. (8), (9) total magnitude and logarithm of the effective radius, from fit with a Sérsic profile; col. (10) Sérsic index, the typical uncertainty is 0.1, while the uncertainties for ID 2015 and 2111 are 0.7; col. (11) position angle of major axis measured from North through East; col. (12) ellipticity.

^a No reliable Sérsic fit can be derived due to scattered light from a nearby source.

SPECTROSCOPIC DATA

Observations and reductions

The spectroscopic reductions were done using the same techniques as described for the nod-and-shuffle data used in Jørgensen & Chiboucas (2013). The only difference is that size and behavior of the charge diffusion effect (CDE) of the the GMOS-N E2V DD CCDs compared to that of the original GMOS-N E2V CCDs. Briefly, the CDE becomes stronger at longer wavelengths and is seen as charge diffused from each individual pixel into all neighboring pixels, see also Abraham et al. (2004) for a description and Jørgensen & Chiboucas (2013) for a figure that shows how the CDE affects spectroscopic data. As explained in that paper, in the absence of a correction the CDE leads to over-subtraction of the sky signal at long wavelengths.

We attempted to use the same technique to correct for the CDE for the E2V DD CCDs as used in Jørgensen & Chiboucas (2013). However, it turns out that the effect for these CCDs not only depends on the wavelength but also on the physical location on the array. We therefore obtained custom calibrations to enable the correction. These calibrations consist of quartz-halogen flat fields taken through the MOS masks. The flat fields are shuffled on the detector the same way as the science observations are obtained. However, in order to avoid saturating the array only one shuffle cycle was used for the shuffled flat fields. At the same time we obtained conventional quartz-halogen flat fields. Using the two types of flat fields together makes it possible to derive a correction image that can be used to correct the flat fields taken with the science observations at night, such that after the correction the flat fields will include the multiplicative effect of the CDE. Due to small flexure effect as well as the fact that the science data are taken with deliberate small offsets in the detector translation stage between exposures, flat fielding for pixel-to-pixel variations should be done with flat fields taken with the science data, rather than simply use the shuffled flat fields obtained after the fact.

The determination of the correction image is done with the following steps:

1. Bias correct of both shuffled and conventional flat field.
2. Fit both flat fields with cubic splines row-by-row and detector-by-detector.
3. Normalize the smooth fits for each slitlet with the fit in the central row of each slitlet. This is also done detector-by-detector.
4. For both flat fields, mosaic the images from the three arrays in GMOS-N.
5. Cut each flat field into slitlets.
6. Ratio the conventional flat field with the shuffled flat field in original position. This will show the CDE affecting the lower part of the lower image of the slitlets.
7. Repeat the steps mosaic, cut and ratio, but with the conventional flat field offset to match the upper image of the flat field in the shuffled flat field. The resulting ratio image will show the CDE affecting the upper part of the upper image of the slitlets.
8. Fit the effect row-by-row with a cubic spline in order to suppress pixel-to-pixel noise in the correction image.
9. Reformat the correction image to match the flat fields, which have six extensions matching the six read-out amplifiers on array.

The calibration was repeated for each of the two wavelength setting used for the science observations, and for each of the two MOS masks. Thus, in total four calibration images were used. We repeated the determination several times over a period of a few weeks to ensure that the calibration did not change in time. No significant time dependence was found. Figure 17 shows a sub-image of the 2-dimensional correction image together with examples of the size of the correction as it affects the science data. The size of the correction depends on the geometry of the slitlets, the placement of the objects in the slitlets, and the extraction aperture. The correction effect shown on Figure 17 matches the configuration used for our data. The CDE calibration is critical for MOS nod-and-shuffle observations using as short slits as done here (2.5 arcsec) and attempting to obtain observations redwards of $\approx 8000\text{\AA}$.

Following the CDE correction, the remainder of the spectroscopic reduction steps are identical to those described in Jørgensen & Chiboucas (2013). The result of the spectroscopic reductions are 1-dimensional extracted spectra calibrated to a relative flux scale. The spectra were median filtered and resampled to just better than critical sampling, cf. Jørgensen & Chiboucas. The instrumental resolution was derived from sky spectra processed exactly the same way as the science spectra. The instrumental resolution for all slitlets is between 2.90 and 3.14 \AA measured as sigma in a Gaussian fit to the sky lines.

Spectroscopic parameters

The calibrated spectra were fit with stellar templates as described in Jørgensen & Chiboucas (2013). This results in determination of the redshifts and the velocity dispersions. The fits were performed with the kinematics fitting software made available by Karl Gebhardt, see Gebhardt et al. (2000, 2003) for a description of the software. Spectra of member galaxies were fit in the wavelength range 3750–4100 \AA . The software fits the spectra in pixel space. The template stars are convolved to the instrumental resolution of the science spectra. Individual values for each slit is used as these are not identical. As in Jørgensen & Chiboucas (2013) we determine the instrumental resolution from stacked sky spectra processed in the same way as the science spectra. The software determines the line-of-sight-velocity-distribution (LOSVD) from the science spectra and then the velocity dispersion is derived from the LOSVD through both a Gauss-Hermite polynomial fit and a Gaussian fit. For the 19 member galaxies with velocity dispersion determined the offset in log space between the two measurements is -0.036 with the Gauss-Hermite polynomial fits giving the smaller velocity dispersions. One may argue that using Gaussian fits is a suitable choice for the RXJ0848.6+4453 data due to the relatively short wavelength range and a median S/N of 18 per \AA ngstrom, making the uncertainties on the higher order terms of the Gauss-Hermite polynomial fit large. However, for consistency with previous work, we use the velocity dispersions derived from the Gauss-Hermite polynomial fits to the LOSVD.

Because the software determines the fits in pixel space, it is straight forward to mask wavelength ranges not to be included in the fit. We used this to flag areas of strong residuals from the sky subtraction, and for ID 2772 also to mask Balmer emission

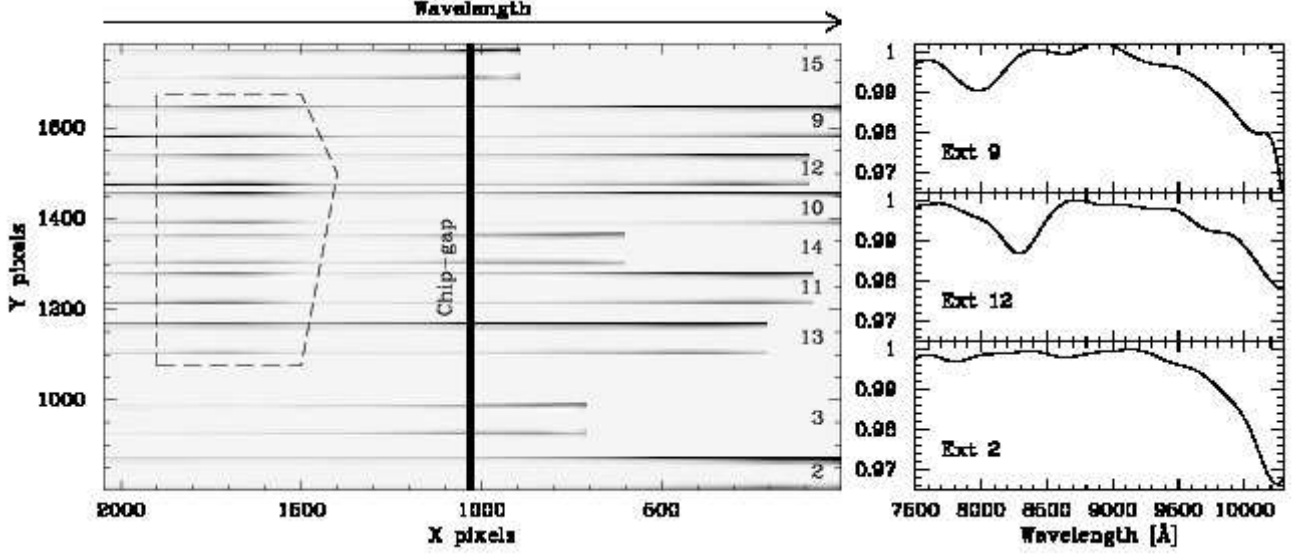


Figure 17. Left panel: Subimage of the CDE correction image. The image is scaled from 0.92 to 1.003. White areas either have insignificant correction (values of ≈ 1) or are between the slitlets. Grey-to-black shows larger effects. Black vertical area – chip gap between CCD1 and CCD2. Each slitlet can be seen on the image as an area near symmetric in the Y-direction as the correction in the upper and lower part of the shuffled image of the slitlet is expected to be identical. The subimage contains nine slitlets, labeled with their extension number. The dashed line marks the approximate area on CCD2 where the CDE varies with spatial location on the CCD, in addition to the variation with wavelength, see text. Right panels: The CDE for three example extensions (2, 9 and 12) as it affects the science data. Extensions 9 and 12 are affected by the area on CCD2 where the CDE varies with spatial location on the CCD.

lines in the fitted wavelength range. None of the other galaxies have significant emission lines within the wavelength range 3750–4100Å. As in Jørgensen & Chiboucas, we use three template stars with spectral types K0III, G1V and B8V. Figure 18 shows the normalized spectra, fits and residuals in the wavelength region covered by the fits. The purpose of the set of template stars is to span the stellar populations in the galaxies. From Figure 18 we conclude that use of these three stars accomplishes this. Further, we choose to use the same template stars as in our previous work to ensure consistency with our previous publications. Aperture correction of the velocity dispersions were performed using the technique from Jørgensen et al. (1995b).

The uncertainties, $\sigma_{\log \sigma}$, on the velocity dispersions are derived by the fitting software using a bootstrap method. In Figure 19 we show the resulting uncertainties versus the S/N of the spectra. The uncertainties scale approximately with S/N as $\sigma_{\log \sigma} \approx 1.2 \times S/N^{-1}$. This relation is shown on the figure.

We have assessed possible systematic errors on the derived velocity dispersions resulting from (1) incorrect instrumental resolution, (2) incorrect telluric correction, and (3) incorrect sky subtraction.

The instrumental resolution varies from slit to slit with the total range being approximately $\pm 4.5\%$. The formal uncertainties on the derived instrumental resolutions as estimated from the rms scatter of measurements of individual skylines in each slit is 1–3%. We estimated the systematics that may be introduced in the velocity dispersion measurements from incorrect determination of the instrumental resolution by refitting all spectra adopting instrumental resolutions of 10% larger and 10% smaller than measured. The median offsets relative to the velocity dispersions listed in Table 11 are less than 0.005 in $\log \sigma$. As this is a factor five less than the intrinsic consistency of 0.026 our low redshift sample (Jørgensen et al. 2005), we conclude that systematic errors from incorrect determination of the instrumental resolution do not affect our results significantly.

The telluric correction was derived from spectra of two blue stars included in the masks. Thus, the calibration spectra were obtained with identical airmass and water vapor as the science spectra and processed in the same way as the science spectra. The combined spectrum of the two blue stars was normalized. We then cleaned the spectrum for noise and stellar features outside the known bands of atmospheric absorption. At wavelengths long than 8500 Å we used an ATRAN model spectrum of the atmospheric absorption (Lord 1992) to guide this cleaning process. Figure 20 shows the normalized spectrum before cleaning, the ATRAN model, and the adopted telluric correction. The wavelength interval for the kinematics fitting is shown in the observed frame. The long wavelength limit of this fitting interval was set to avoid the strong telluric absorption bands redwards of ≈ 9300 Å. As the spectra used to determine the telluric correction are obtained simultaneously with the science, there can be no mismatch in airmass or water vapor. Nevertheless, we tested the effect of the telluric correction being systematically wrong with 10% by correcting the spectra with the telluric correction test spectrum derived from the measured telluric correction spectrum as

$$\text{telluric}_{\text{test}} = 1 - X(1 - \text{telluric}_{\text{measured}}) \quad (\text{B1})$$

with $X = 0.9$ and 1.1 , respectively. The spectra were then flux calibrated, resampled, normalized, processed with the kinematics fitting software. The resulting velocity dispersions are in both cases consistent with those presented in Table 11 with median zero point offsets of < 0.003 for the two cases and rms scatter of 0.04 in $\log \sigma$ for the 19 member galaxies with measured velocity dispersions.

Finally we assessed the systematic effects on the velocity dispersions from a possible incorrect sky subtraction. The data are obtained in nod-and-shuffle mode to limit such sky subtraction errors. Within the wavelength fitting interval (3750–4100 Å in the

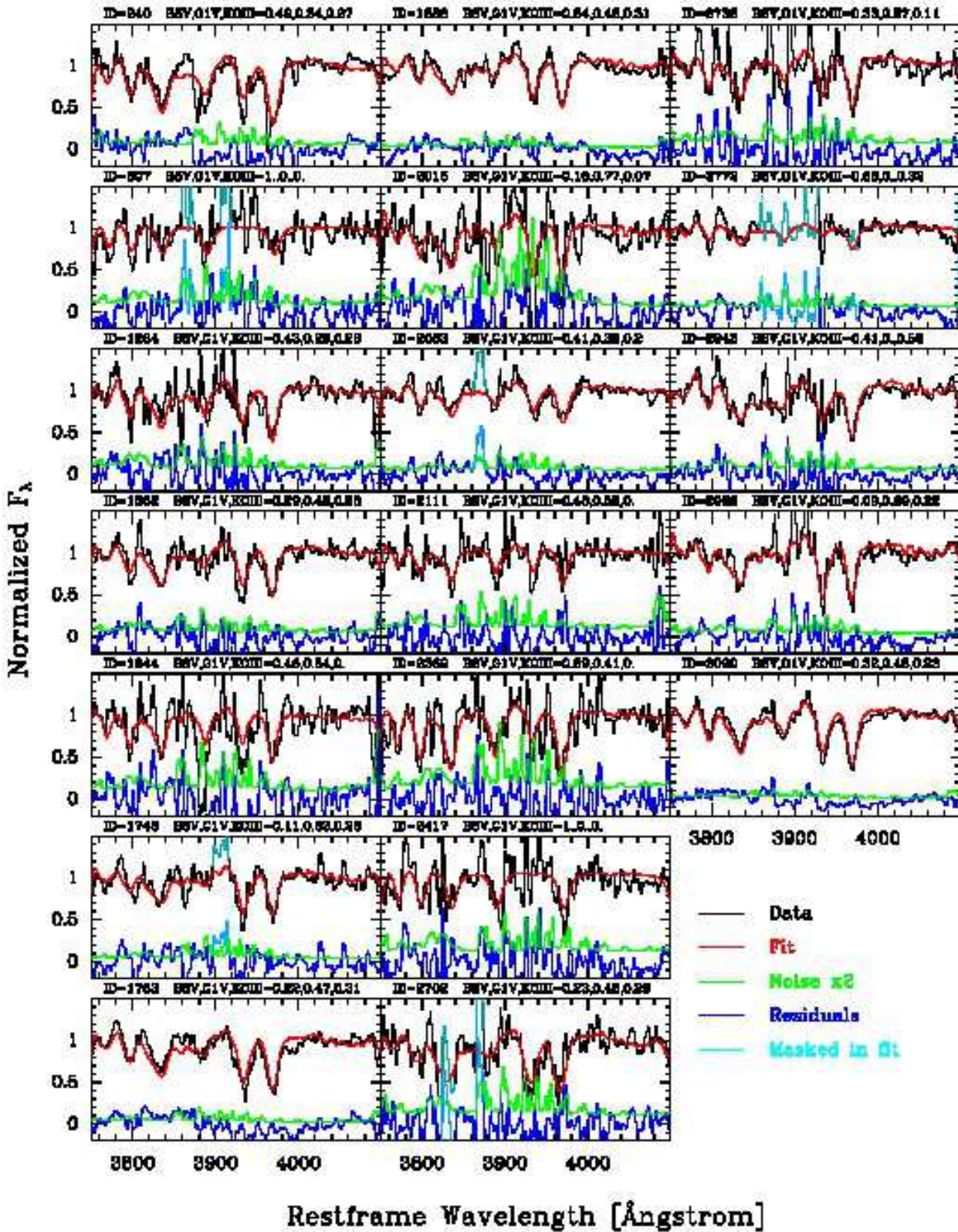


Figure 18. Summary of the kinematics fitting for the members of RXJ0848.6+4453 for which determination of the velocity dispersion was possible. Black – normalized spectra; red - best fit; green – noise times two, normalized the same way as the spectra; blue - residuals from the best fit; cyan – wavelength regions excluded from the fits due to strong sky subtraction residuals. The figure shows the general quality of the fits and demonstrates that the use of the three template stars adequately spans the stellar populations present in the sample.

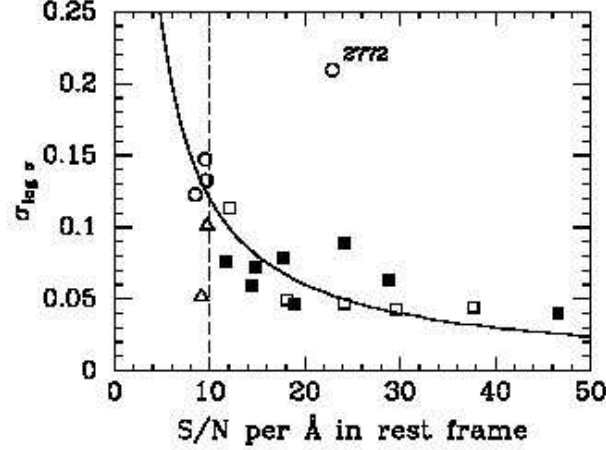


Figure 19. The uncertainty on the velocity dispersions as derived using a bootstrap method versus the S/N per \AA in the rest frame of the galaxies. Solid squares – bulge-dominated galaxies with $EW[O II] \leq 5 \text{\AA}$; open squares – bulge-dominated galaxies with $EW[O II] > 5 \text{\AA}$; triangles - bulge-dominated galaxies with $S/N < 10$; circles – disk-dominated galaxies. Galaxy ID 2772 marked on the figure is an irregular galaxy, see imaging on Figure 22, for which masking of residuals from the sky subtraction affected the available wavelength range significantly, cf. Figure 18. Solid line – approximate relation between S/N and $\sigma_{\log \sigma}$: $\sigma_{\log \sigma} \approx 1.2 \times S/N^{-1}$. Dashed vertical line – $S/N=10$. Galaxies below this S/N cutoff are excluded from the determination of relations and zero points.

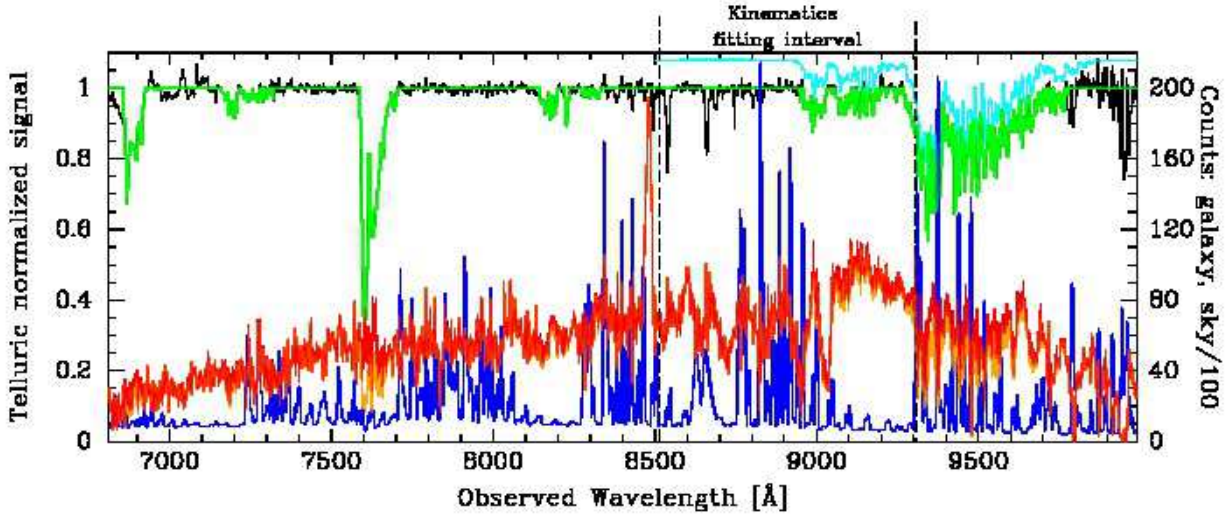


Figure 20. Telluric correction and typical sky spectrum for illustration shown together with the spectrum of the brightest cluster member observed. Black - combined spectra of the two blue stars in the masks. Cyan – ATRAN model (Lord 1992) for water vapor of 2 mm and elevation of 45 degrees at the altitude of Gemini North. The model has been resampled and convolved to match the spectral sampling and instrumental resolution of our data. The model is offset 0.08 from the data for clarity. Green – adopted telluric correction. Orange – uncalibrated spectrum (in counts) of the brightest cluster member observed ID 1763. Red – spectrum (in counts) of ID 1763 after telluric correction. Blue – sky spectrum matching ID 1763, divided by 100. See text for discussion of the figure.

rest frame) even for the brightest cluster member observed, ID 1763, the signal from the galaxy is only 2.6% of the average sky signal. Figure 20 illustrates this by showing the spectrum of ID 1763 in counts together with the matching sky spectrum scaled down with a factor 100. We tested the effect of the sky subtraction being over- or under-subtracted with 0.1%. An error in the sky subtraction of this size cause visible systematic residuals in the resulting spectra within the wavelength region used for the kinematics fitting. We therefore view this as the upper limit on the possible systematic error in the sky subtraction. The spectra were then processed through the remainder of the processing steps and velocity dispersions derived. Comparing the resulting velocity dispersions to those presented in Table 11 for the 19 member galaxies with measured velocity dispersions we find median offsets in $\log \sigma$ of < 0.015 in the two cases. The rms scatter in $\log \sigma$ for over- and under-subtraction of the sky is 0.13 and 0.05, respectively. If limiting the comparison to the 13 bulge-dominated galaxies with $S/N \geq 10$, the scatter decreases to 0.08 and 0.03, respectively. These 13 galaxies are the galaxies included in our analysis of the size and velocity dispersion evolution as well as the FP analysis.

We conclude that systematic errors on the the measured velocity dispersions due to the determination of the instrumental resolution, the adopted telluric correction or the sky subtraction do not affect our results significantly.

Our ability to determine line indices from the spectra are limited by the sky subtraction errors, which in turn to a large extent are a result of the imperfect correction for the CDE. While the spectra cover wavelengths to 4400\AA in the rest frame, the sky

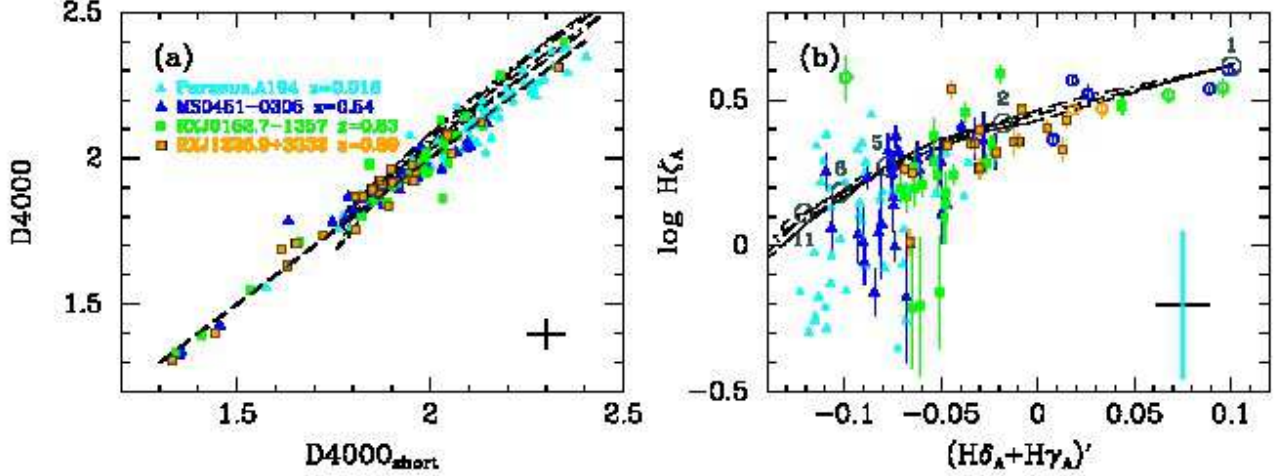


Figure 21. (a) Calibration of $D4000_{\text{short}}$ to consistency with $D4000$. Typical measurement uncertainties are shown based on repeat measurements (see Jørgensen & Chiboucas 2013 for details). Cyan points – Perseus, A194; Blue points – MS0451–0305; green points – RXJ0152.7–1357; orange points – RXJ1226.9+3332. Thick dashed line – one-to-one relation, scatter relative to this relation is 0.046 in $D4000$. Thin dashed and dotted lines – predictions based on deriving the indices from the model SEDs from Maraston & Strömbäck (2011). (b) Higher order Balmer line indices versus each other. $(H\delta_A + H\gamma_A)' \equiv -2.5 \log(1 - (H\delta_A + H\gamma_A)/(43.75 + 38.75))$, see Kuntschner (2000). The typical measurement uncertainty on $(H\delta_A + H\gamma_A)'$ is shown in the lower right of the panel. The adopted value of 0.014 is based on the internal comparison of repeat measurements presented in Jørgensen & Chiboucas (2013). For $H\zeta_A$ we show individual uncertainties for the $z = 0.5 - 1$ clusters as these vary significantly as a function of the strength of the line. For the low redshift sample the median uncertainty on $\log H\zeta_A$ is 0.26, as shown on the figure. Symbols as on panel (a), except galaxies with Sérsic index less than 1.5 are shown as open circles. Thin dashed and dotted lines – predictions based on deriving the indices from the model SEDs from Maraston & Strömbäck. Open circles on the model lines correspond to the models with solar $[M/H]$ and ages in Gyr as labeled, see text for discussion.

subtraction errors limit the range for which the spectra can be used for determination of absorption line indices to $\approx 4075\text{\AA}$ in the rest frame (9250\AA observed). We have derived the following indices CN3883, CaHK, $D4000$ and $H\zeta_A$. We have adopted the bandpass definition for the higher order Balmer line $H\zeta$ from Nantais et al. (2013). The index is named $H6_A$ in Nantais et al., while we opt to name it after the name of the Balmer line it is measuring.

The red bandpass of the original definition of the $D4000$ index (Gorgas et al. 1999) is in our spectra severely affected by the sky subtraction errors. We have therefore defined a shorter red bandpass in order to be able to measure the equivalent of the $D4000$ index. We call this index $D4000_{\text{short}}$ and define it as

$$D4000_{\text{short}} = 1.2107(200/75) \left(\int_{4000(1+z)}^{4075(1+z)} f_{\lambda} d\lambda \right) \left(\int_{3750(1+z)}^{3950(1+z)} f_{\lambda} d\lambda \right)^{-1} - 0.092 \quad (\text{B2})$$

The definition ensures that on average $D4000_{\text{short}} = D4000$. The factor $(200/75)$ reflects the difference in the length of the two passbands in the definition, as the original $D4000$ index has identical length passbands. Figure 21a shows the two indices versus each other for our sample of member galaxies in Perseus, A194, MS0451–0305, RXJ0152.7–1357, and RXJ1226.9+3332. The figure also shows the indices determined from the model SEDs from Maraston & Strömbäck (2011). The rms scatter of the data points relative to the one-to-one relation is 0.046. In Jørgensen & Chiboucas we estimated that the measurement uncertainty on $D4000$ for our $z = 0.5$ and $z = 0.9$ data is 0.051 and 0.033, respectively. Thus, the internal scatter of the relation between $D4000$ and $D4000_{\text{short}}$ is insignificant, and we will assume that $D4000_{\text{short}}$ has a similar uncertainty as that of $D4000$.

Our data for RXJ0848.6+4453 do not allow us to stack the frames in subsets for the full data set in order to derive better estimate uncertainties on the spectroscopic parameters. However, in the wavelength region 3750\AA to 4100\AA the median S/N of the data is similar to that of our spectra for MS0451.6–0305 (Jørgensen & Chiboucas 2013). We therefore adopt the uncertainties for CN3883, \log CaHK and $D4000$ from that paper (Table 19 in that paper). The values are 0.035, 0.060 and 0.051 for CN3883, \log CaHK and $D4000$, respectively. The uncertainty on $H\zeta_A$ depends too strongly on the strength of the index to be adequately represented by one value. Thus, we show individual error bars on figures using this index, except for the low redshift sample for which we for clarity show the median uncertainty. The low redshift sample spectra have fairly low S/N in the wavelength region of $H\zeta$. That combined with the weak strength of the line for these galaxies leads to a high relative uncertainty, typically 0.26 on $\log H\zeta_A$. The line indices have been aperture corrected and corrected for velocity dispersion as described in Jørgensen et al. (2005), see Jørgensen & Chiboucas (2013) for a discussion of the method applied to intermediate redshift galaxies. As for the lower order Balmer lines, we assume that $H\zeta_A$ has no aperture correction.

As $H\zeta_A$ is the only Balmer line index measurable from our RXJ0848.6+4453 data, we have used the data for the three $z < 1$ clusters as well as model SEDs from Maraston & Strömbäck (2011) to evaluate to what extent this index is suitable for estimating ages. In Figure 21b we show the indices for the high order Balmer lines versus each other for the low redshift sample and three $z < 1$ clusters. Model predictions based on the model SEDs from Maraston & Strömbäck are overplotted. $H\zeta_A$ is useful as an indicator of very young stellar populations, ages of 2 Gyr or less. The ages of the older stellar populations are difficult to measure using $H\zeta_A$ due to the uncertainties affecting our data.

The mix of the three template stars in our best fit models from the kinematics fitting as expected correlate with the $H\zeta_A$ and CaHK indices in the sense that the B8V fraction in the best fit model increases with increasing $H\zeta_A$, while the sum of the G1V and K0III fractions increases with increasing CaHK. However, because stellar population models already exist to assist the interpretation of the index strengths and no such modeling exist for the template stars, we will use only the indices in our analysis of the data.

For galaxies with detectable emission from [O II] we determined the equivalent width as well as the (relative) flux of the [O II] $\lambda\lambda$ 3726,3729 doublet. With an instrumental resolution of $\sigma \approx 3 \text{ \AA}$ (FWHM $\approx 7 \text{ \AA}$), the doublet is not resolved in our spectra and we refer to it simply as the “[O II] line”.

Tables 11 and 12 list the results from the template fitting and the derived line strengths.

PRESENTATION OF THE IMAGING AND SPECTRA FOR RXJ0848.6+4453

The spectra as well as stamp-sized images of the galaxies from the *HST*/ACS imaging of the cluster members are shown in Figure 22. The stamps cover the equivalent of $75 \text{ kpc} \times 75 \text{ kpc}$ at the distance of the cluster. The spectra used to create Figure 22 are available in the online journal.

Table 11
RXJ0848.6+4453: Results from Template Fitting

ID	Redshift	Member ^a	$\log \sigma$	$\log \sigma_{\text{cor}}^b$	$\sigma_{\log \sigma}$	Template fractions			χ^2	S/N ^c
						B8V	G1V	K0III		
240	1.2607	1	2.452	2.476	0.046	0.49	0.24	0.27	3.2	18.9
336	...	2	5.3
361	1.3285	0	2.346	2.370	0.060	0.00	0.87	0.13	4.2	23.2
438	1.3276	0	2.8
634	1.3255	0	5.1
654	1.2610	1	2.9
661	0.8455	0	2.216	2.239	0.059	0.20	0.80	0.00	7.2	61.8
722	1.1374	0	8.5
807	1.2699	1	2.241	2.265	0.114	1.00	0.00	0.00	2.1	12.1
887	0.7160	0	8.7
1044	0.5440	0	2.631	2.651	0.057	0.25	0.00	0.75	1.7	17.0
1045	0.4328	0	8.9
1123	1.2701	1	6.8
1173	1.1162	0	12.4
1177	1.2346	0	2.205	2.229	0.187	0.70	0.30	0.00	1.9	10.8
1264	1.2730	1	1.975	2.000	0.072	0.43	0.29	0.28	1.6	14.8
1276	1.0100	0	10.5
1352	1.3174	0	2.6
1362	1.2729	1	2.394	2.418	0.049	0.29	0.48	0.23	2.3	18.1
1517	1.1429	0	17.1
1533	1.2779	1	4.4
1644	1.2729	1	1.994	2.018	0.147	0.46	0.54	0.00	2.4	9.5
1698	1.1419	0	7.5
1748	1.2698	1	2.262	2.286	0.064	0.11	0.63	0.26	4.0	28.8
1763	1.2749	1	2.328	2.352	0.043	0.22	0.47	0.31	6.2	29.5
1809	1.2686	1	9.5
1888	1.2771	1	2.227	2.251	0.044	0.24	0.45	0.31	4.4	37.7
2015	1.2676	1	2.079	2.103	0.101	0.16	0.77	0.07	2.6	9.8
2063	1.2671	1	2.360	2.384	0.047	0.41	0.39	0.20	1.8	24.1
2111	1.2798	1	2.054	2.078	0.076	0.48	0.52	0.00	1.1	11.6
2138	1.1363	0	8.5
2336	0.8731	0	2.389	2.412	0.044	0.33	0.49	0.18	2.4	41.9
2342	1.2265	0	3.4
2369	1.2667	1	2.210	2.234	0.122	0.59	0.41	0.00	0.8	8.5
2417	1.2636	1	2.195	2.219	0.132	1.00	0.00	0.00	1.4	9.6
2450	1.1366	0	2.351	2.375	0.092	0.00	0.79	0.21	2.8	8.9
2497	1.0823	0	5.8
2600	1.2287	0	2.219	2.243	0.095	0.19	0.39	0.42	2.1	13.4
2624	...	2	6.9
2651	1.2278	0	2.440	2.464	0.101	0.62	0.21	0.16	2.0	23.1
2702	1.2645	1	2.558	2.582	0.052	0.23	0.48	0.29	1.4	9.1
2735	1.2669	1	2.268	2.292	0.059	0.33	0.57	0.11	1.9	14.4
2772	1.2706	1	2.132	2.156	0.209	0.68	0.00	0.32	3.1	22.9
2943	1.2677	1	2.169	2.193	0.078	0.41	0.00	0.59	1.6	17.7
2989	1.2643	1	2.044	2.068	0.089	0.09	0.69	0.22	3.0	24.2
3030	1.2272	0	2.268	2.292	0.057	0.51	0.49	0.00	2.0	14.5
3074	1.1407	0	2.180	2.203	0.081	0.25	0.42	0.33	2.2	21.6
3090	1.2780	1	2.320	2.344	0.040	0.32	0.45	0.23	7.8	46.6
3144	1.3192	0	13.3
3384	1.1954	0	7.7
3426	1.2756	1	6.2
3461	0.6546	0	12.0
3505	0.5700	0	30.0
9001	1.0745	0	4.1

^a Adopted membership: 1 – galaxy is a member of RXJ0848.6+4453; 0 – galaxy is not a member of RXJ0848.6+4453; 2 – redshift cannot be determined.

^b Velocity dispersions corrected to a standard size aperture equivalent to a circular aperture with diameter of 3.4 arcsec at the distance of the Coma cluster.

^c S/N per Ångstrom in the rest frame of the galaxy. The wavelength interval was chosen based on the redshift of the galaxy as follows: redshift 1.00-1.35 – 3750-4100 Å; redshift 0.60-1.00 – 4100-4600 Å; redshift <0.60 – 4600-5200 Å. For ID 336 and ID 2624 a redshift of 1.27 was assumed for the S/N calculation.

Table 12
RXJ0848.6+4453: Line Indices and [O II] for Cluster Members

ID	CN3883	σ_{CN3883}	CaHK	σ_{CaHK}	D4000 ^a	σ_{D4000}	H ζ_{A}	$\sigma_{\text{H}\zeta_{\text{A}}}$	EW [O II]	$\sigma_{\text{EW[OII]}}$	flux([O II]) ^b	$\sigma_{\text{flux([OII]}}$
240	0.097	0.013	26.60	0.65	2.169	0.015	7.85	0.24	5.0	2.0	1.23	0.19
654	183.5	102.9	4.10	0.40
807	44.1	2.5	6.43	0.15
1123	155.7	123.5	5.97	0.32
1264	2.139	0.019	2.9	0.6	0.57	0.11
1362	0.179	0.013	18.37	0.73	1.962	0.014	3.32	0.34	15.6	2.7	3.57	0.14
1533	25.9	8.3	2.93	0.17
1644	14.00	1.59	2.115	0.030	12.68	0.37	9.9	2.6	1.77	0.20
1748	0.122	0.009	22.59	0.50	2.291	0.011	2.90	0.25
1763	0.202	0.008	22.41	0.40	2.366	0.010	3.06	0.23	17.0	0.5	8.36	0.16
1809	24.2	9.9	2.10	0.14
1888	0.158	0.007	19.19	0.34	2.164	0.007	2.09	0.20	9.1	0.3	5.36	0.17
2015	3.154	0.042
2063	0.070	0.010	13.85	0.62	1.893	0.010	3.65	0.25	14.6	2.2	4.63	0.14
2111	0.113	0.021	11.41	1.24	1.704	0.019	4.62	0.51	8.0	1.0	1.81	0.15
2369	0.099	0.030	20.23	1.63	2.103	0.033	6.64	0.58	29.6	8.4	1.88	0.16
2417	0.116	0.023	1.544	0.021	4.69	0.48	40.8	6.5	7.29	0.30
2702	0.156	0.026	27.68	1.49	2.136	0.031	4.29	0.62
2735	0.089	0.016	14.51	1.04	1.853	0.017	1.99	0.40	3.5	0.9	0.91	0.11
2772	1.568	0.009	32.3	1.4	10.29	0.15
2943	0.188	0.014	19.82	0.77	2.081	0.015	2.60	0.39
2989	2.165	0.012	1.9	0.3	0.67	0.11
3090	0.174	0.005	19.99	0.27	2.065	0.006	4.17	0.14

Note. — The indices have been corrected for galaxy velocity dispersion and aperture corrected.

^a Measured as D4000_{short}, cf. Eq. B2.

^b Relative flux in 10^{-15} ergs cm⁻² sec⁻¹ Å⁻¹ measured within the spectral aperture.

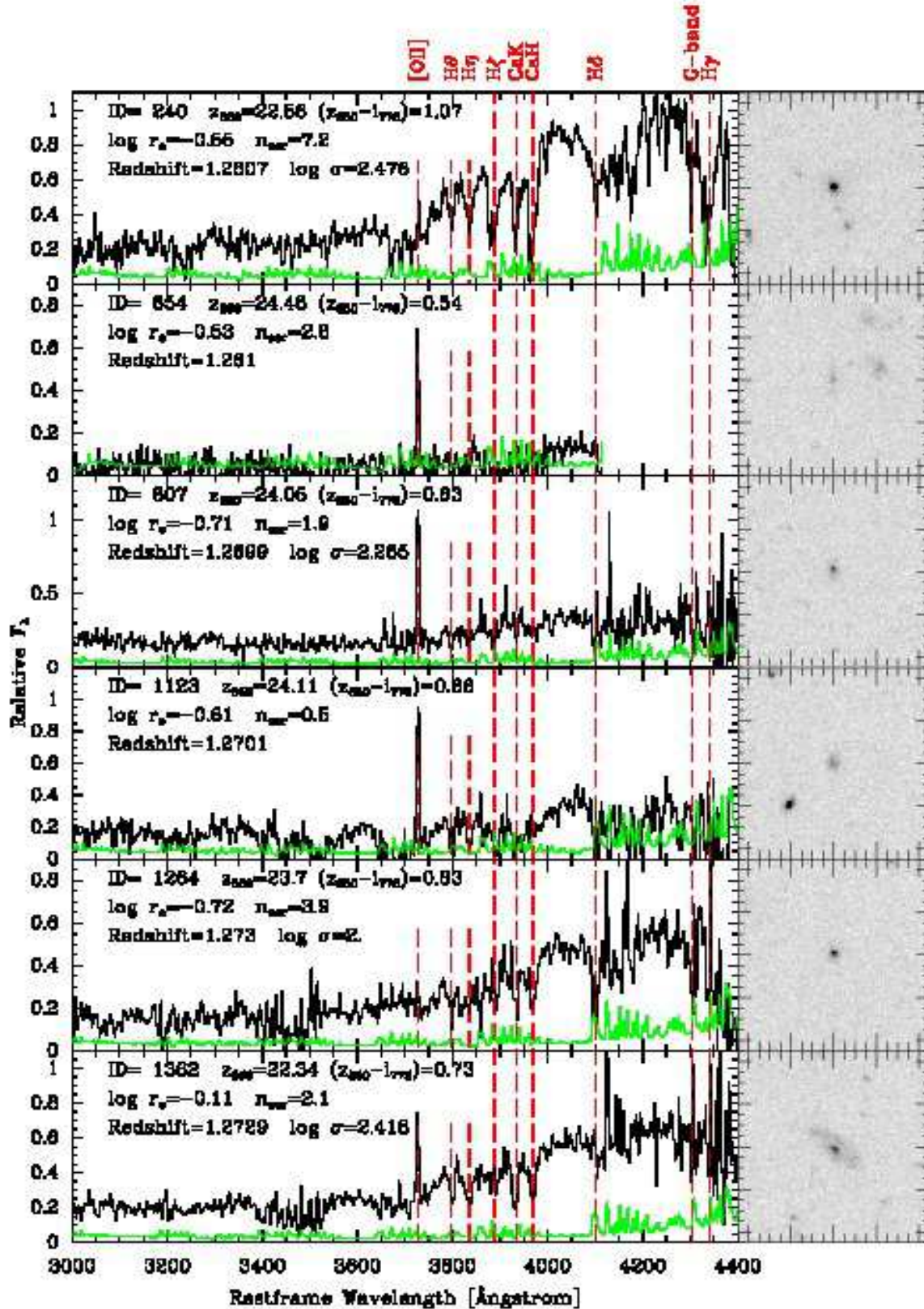


Figure 22. Spectra and grey scale images of the galaxies that are considered members of RXJ0848.6+4453. On the spectra, black lines show the galaxy spectra, green lines show the random noise multiplied with two. At the strong sky lines, the random noise underestimates the real noise due to systematic errors in the sky subtraction. Some of the absorption lines are marked. The location of the emission line [O II], is also marked, though emission is only present in some of the galaxies. The spectra shown in this figure have been processed as described in the text, including resampling to just better than critical sampling. The grey scale images are made from the *HST*/ACS images of the RXJ0848.6+4453 sample in the F850LP filter. Each image is 9 arcsec \times 9 arcsec. At the distance of RXJ0848.6+4453 this corresponds to 75 kpc \times 75 kpc for our adopted cosmology. North is up, East to the left.

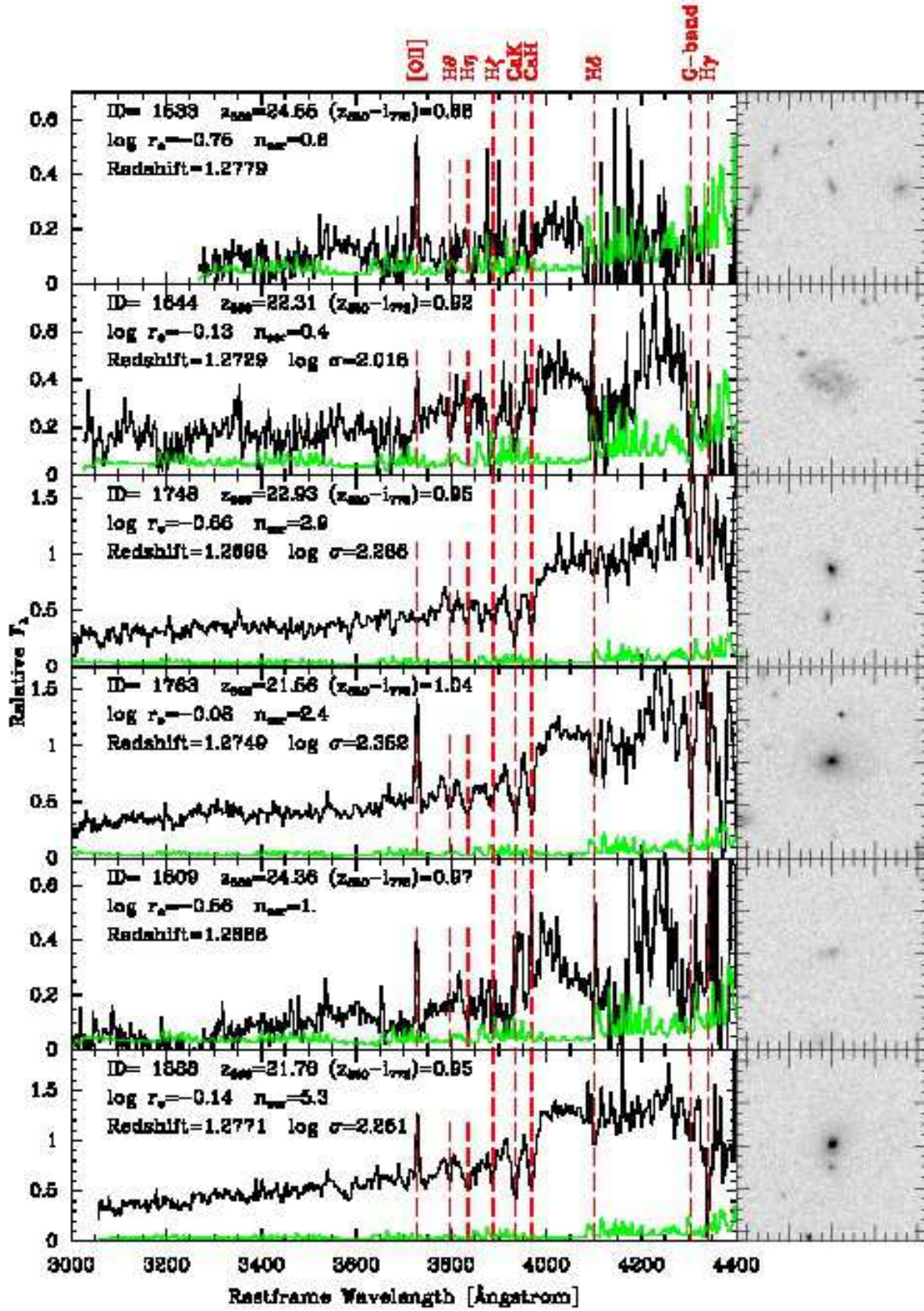


Fig. 22 – Continued.

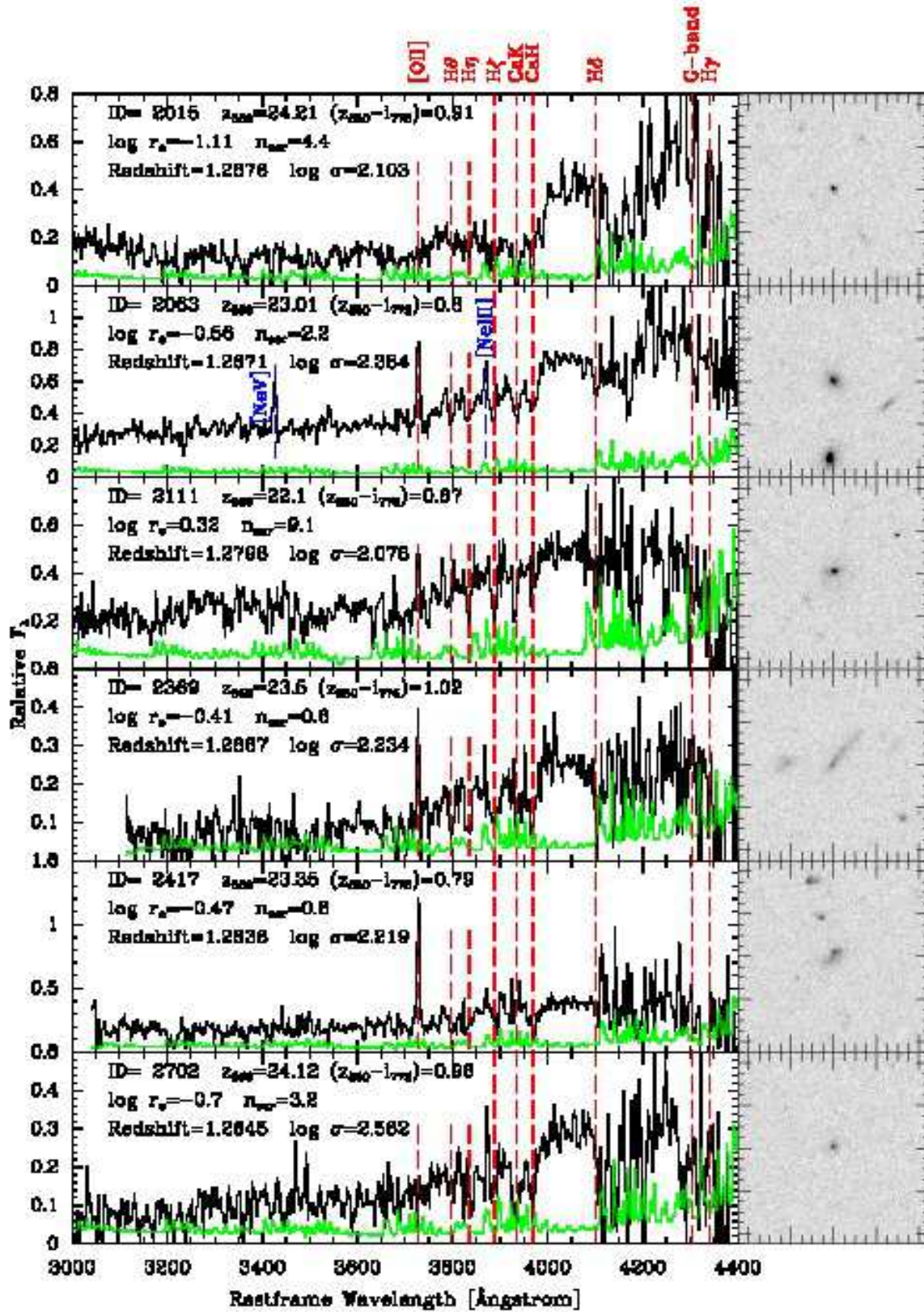


Fig. 22 - Continued.

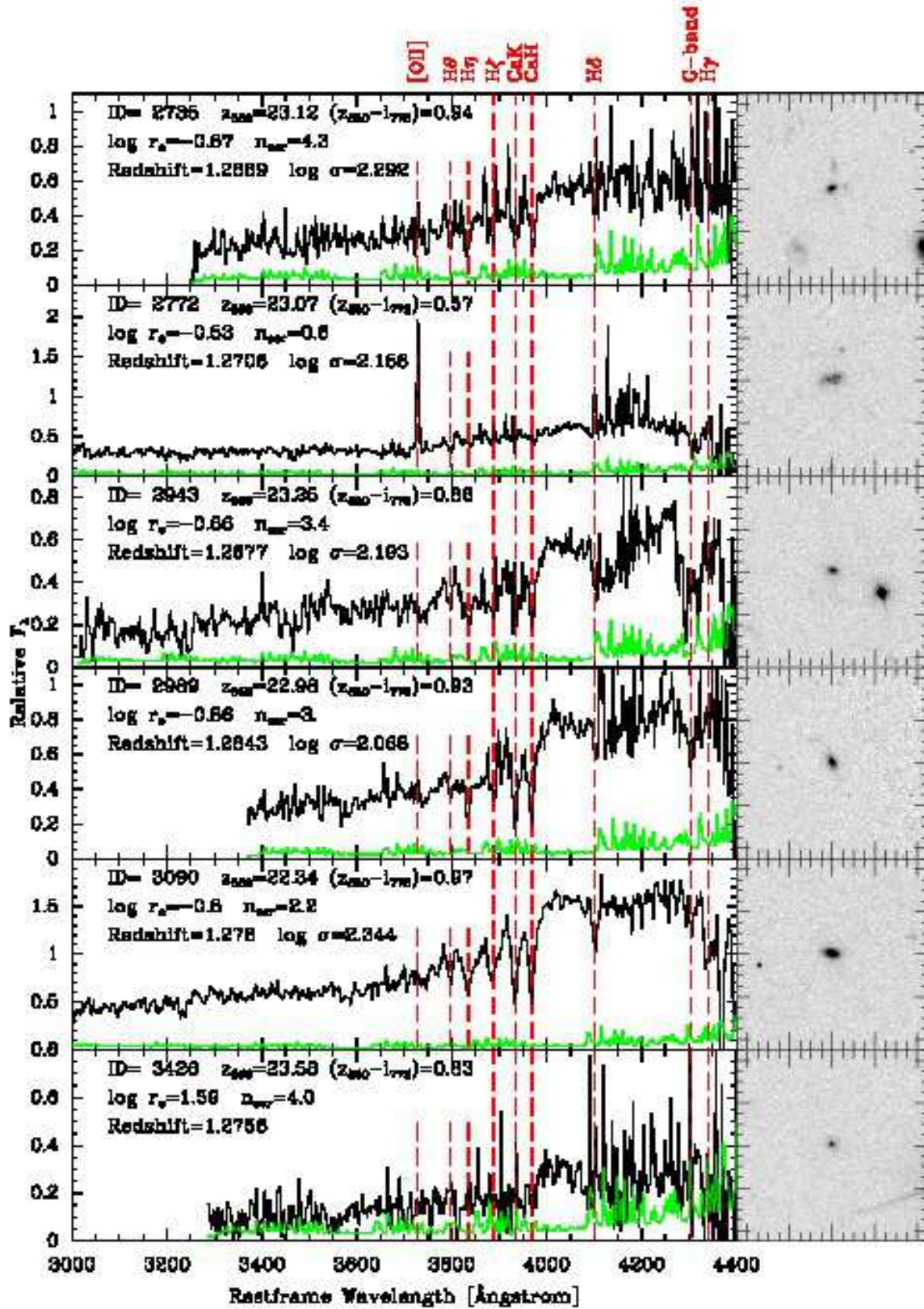


Fig. 22 – Continued.